

¹
² Susceptible host dynamics explain pathogen resilience to
³ perturbations

⁴
⁵ Sang Woo Park^{1,*} Bjarke Frost Nielsen² Emily Howerton² Bryan T. Grenfell^{2,3,4}
⁶ Sarah Cobey¹

⁷ **1** Department of Ecology and Evolution, University of Chicago, Chicago, IL, USA

⁸ **2** Department of Ecology and Evolutionary Biology, Princeton University,
Princeton, NJ, USA

¹⁰ **3** High Meadows Environmental Institute, Princeton University, Princeton, NJ,
¹¹ USA

¹² **4** Princeton School of Public and International Affairs, Princeton, NJ, USA

¹³ *Corresponding author: swp2@uchicago.edu

¹⁴ **Abstract**

¹⁵ A major priority for epidemiological research in a time of anthropogenic change is
¹⁶ understanding how infectious disease dynamics respond to perturbations. Interven-
¹⁷ tions to slow the spread of SARS-CoV-2 significantly disrupted the transmission
¹⁸ of other human pathogens. As interventions lifted, whether and when respiratory
¹⁹ pathogens would eventually return to their pre-pandemic dynamics remains to be
²⁰ answered. Here, we present a framework for estimating pathogen resilience based
²¹ on how fast epidemic patterns approach their pre-pandemic, endemic dynamics and
²² analyze relevant time series data from Hong Kong, Canada, Korea, and the US. By
²³ quantifying the resilience of common respiratory pathogens, we are able to predict
²⁴ when each pathogen will eventually return to its pre-pandemic dynamics. Our pre-
²⁵ dictions closely match the observed deviations (or lack thereof) from the pre-COVID
²⁶ dynamics of respiratory pathogens. Discrepancies between predicted and observed
²⁷ dynamics indicate the long-term impacts of pandemic perturbations, suggesting that
²⁸ some pathogens may be converging to a different endemic cycle. Finally, we show
²⁹ that the replenishment rate of the susceptible population is a key determinant of
³⁰ pathogen resilience, which in turn determines the sensitivity of a system to stochas-
³¹ tic perturbations. Overall, our analysis highlights the persistent nature of common
³² respiratory pathogens compared to vaccine-preventable infections, such as measles.

Introduction

34 Non-pharmaceutical interventions to slow the spread of SARS-CoV-2 disrupted the
 35 transmission of other human respiratory pathogens, adding uncertainties to their future
 36 epidemic dynamics and their public health burden [1]. As interventions lifted,
 37 large heterogeneities in outbreak dynamics were observed across different pathogens
 38 in different countries, with some pathogens exhibiting earlier and faster resurgences
 39 than others [2, 3, 4]. Heterogeneities in the overall reduction in transmission and the
 40 timing of re-emergence likely reflect differences in intervention patterns, pathogen
 41 characteristics, immigration/importation from other countries, and pre-pandemic
 42 pathogen dynamics [5]. Therefore, comparing the differential impact of the pandemic
 43 perturbations across pathogens can provide unique opportunities to learn about underly-
 44 ing pathogen characteristics across different populations, such as their trans-
 45 missibility or duration of immunity, from heterogeneities in re-emergence patterns
 46 [6].

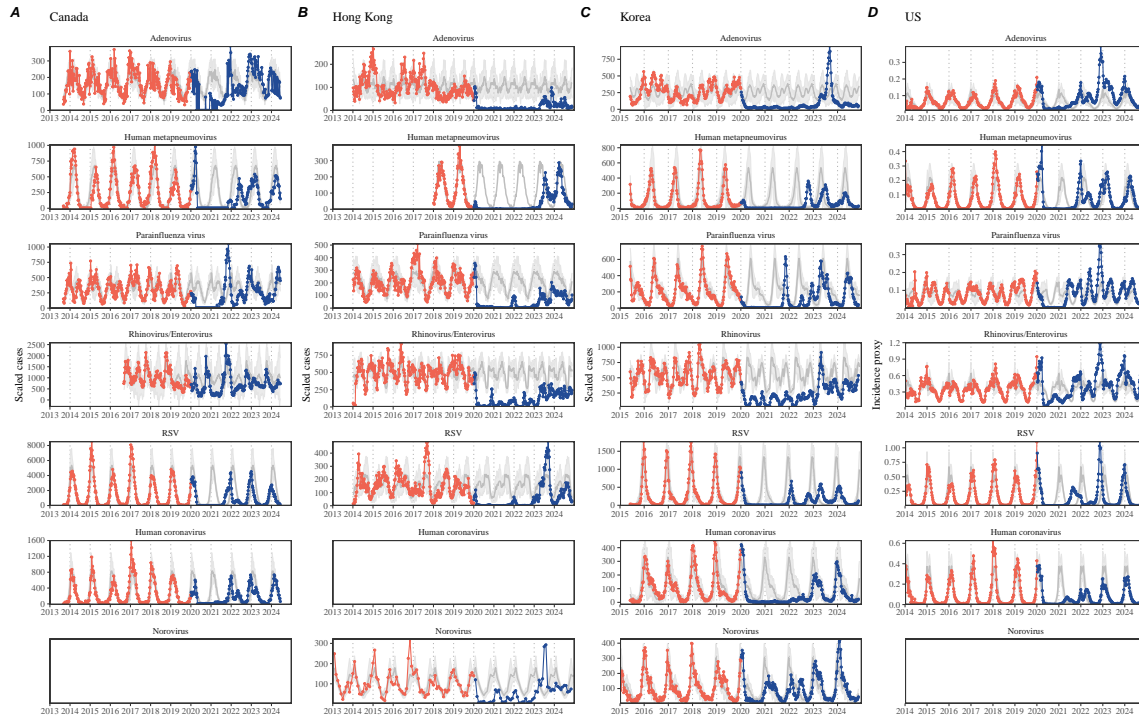


Figure 1: **Observed heterogeneity in responses to pandemic perturbations across respiratory pathogens and norovirus in (A) Canada, (B) Hong Kong, (C) Korea, and (D) US.** Red points and lines represent data before 2020. Blue points and lines represent data since 2020. Gray lines and shaded regions represent the mean seasonal patterns and corresponding 95% confidence intervals around the mean. Mean seasonal patterns were calculated by aggregating cases before 2020 into 52 weekly bins and taking the average in each week. Cases were scaled to account for changes in testing patterns (Materials and Methods).

47 Even though more than five years have passed since the emergence of SARS-CoV-
48 2, we still observe persistent changes in pathogen dynamics following the pandemic
49 perturbations. For example, compared to pre-pandemic, seasonal patterns, human
50 metapneumovirus in Korea seems to circulate at lower levels, whereas RSV in Ko-
51 rea seems to exhibit different seasonality (Figure 1). These observations suggest
52 the possibility of a long-term change in pathogen dynamics following the pandemic
53 perturbations, which might be driven by a long-term shift in human behavior or
54 population-level immunity [7, 8]. For example, the emergence of SARS-CoV-2 could
55 have caused a long-term shift in population-level immunity through its interactions
56 with other pathogens [9], especially with seasonal coronaviruses [7, 10, 11]. The pos-
57 sibility of a long-lasting impact of the pandemic perturbations poses an important
58 question for future infectious disease dynamics: can we predict whether and when
59 other pathogens will eventually return to their pre-pandemic dynamics?

60 So far, most analyses of respiratory pathogens after pandemic perturbations have
61 focused on characterizing the timing of rebound [1, 12, 5]. Instead, we seek to char-
62 acterize how fast (and whether) a pathogen returns to its pre-pandemic dynamics.
63 These two concepts have a subtle but important difference. For example, it took
64 more than 3 years for human metapneumovirus to rebound in Hong Kong, but the
65 observed epidemic patterns in 2024 appear similar to the pre-pandemic seasonal
66 mean, suggesting a possible return to pre-pandemic dynamics, though confirmation
67 may require multiple seasons (Figure 1). Measuring this rate of return is useful be-
68 cause it allows us to quantify the ecological resilience of a host-pathogen system,
69 which can inform responses to future interventions [13, 14, 15, 16].

70 In this study, we lay out theoretical and statistical approaches to characterizing
71 the resilience of a host-pathogen system based on how fast the system recovers from
72 perturbation. We begin by laying out a few representative scenarios that capture
73 the potential impact of pandemic perturbations on endemic pathogen dynamics and
74 illustrate how resilience can be measured by comparing the pre- and post-pandemic
75 dynamics of susceptible and infected hosts. In practice, information on susceptible
76 hosts is often unavailable, making this theoretical approach infeasible. Instead, we
77 utilize a mathematical technique to reconstruct attractors from the data [17], which
78 allows us to measure the rate at which the host-pathogen system approaches this
79 empirical attractor after a perturbation; we define this rate to be the empirical
80 resilience of the host-pathogen system. We use this method to analyze pathogen
81 surveillance data for respiratory and non-respiratory pathogens from Canada, Hong
82 Kong, Korea, and the US. Finally, we show that susceptible host dynamics explain
83 variation in pathogen resilience and demonstrate that more resilient pathogens will be
84 less sensitive to perturbations caused by demographic stochasticity, thereby providing
85 a direct link between pathogen resilience and persistence.

86 **Conceptual introduction to pathogen resilience**

87 In the classical ecological literature, the resilience of an ecological system is measured
88 by the rate at which the system returns to its reference state following a perturbation
89 [13, 14, 15, 16]. This rate corresponds to the largest real part of the eigenvalues of
90 the linearized system near equilibrium—here, we refer to this value as the *intrinsic*
91 resilience of the system, which represents the expected rate of return from perturbed
92 states. In practice, we rarely know the true model describing the dynamics of com-
93 mon respiratory pathogens, limiting our ability to infer the intrinsic resilience of a
94 system. Instead, we can measure the *empirical* resilience of a host-pathogen system
95 by looking at how fast the system returns to the pre-perturbation endemic dynamics
96 after the perturbation has ended. The COVID-19 pandemic provides a crucial exam-
97 ple of a major perturbation, providing unique opportunities to measure the resilience
98 of a host-pathogen system across different countries.

99 **Resilience of a single-strain system under a short-term perturbation.**
100 As an example, we begin with a simple Susceptible-Infected-Recovered-Susceptible
101 (SIRS) model with seasonally forced transmission and demography (i.e., birth and
102 death). The SIRS model is the simplest model that allows for the waning of immunity
103 and is commonly used for modeling the dynamics of respiratory pathogens [18]. First,
104 consider a pandemic perturbation that reduces transmission by 50% for 6 months
105 starting in 2020, which causes epidemic patterns to deviate from their original stable
106 annual cycle for a short period of time and eventually come back (Figure 2A). To
107 measure the resilience of this system empirically, we first need to be able to measure
108 the distance from its pre-pandemic attractor, which is defined as a set of points in
109 state space or phase plane that the system is pulled towards [19]. There are many
110 ways we can measure the distance from the attractor, but for illustrative purposes, we
111 choose one of the most parsimonious approaches: we look at how the susceptible (S)
112 and infected (I) populations change over time and measure the Euclidean distance on
113 the SI phase plane, using the counterfactual unperturbed phase plane as a reference
114 (Figure 2B; Materials and Methods). In this simple case, the locally estimated
115 scatterplot smoothing (LOESS) fit indicates that the distance from the attractor
116 decreases exponentially (linearly on a log scale) with time on average (Figure 2C).
117 Furthermore, the overall rate of return approximates the intrinsic resilience of the
118 seasonally unforced system (Figure 2C).

119 **Resilience of a single-strain system under a long-term perturbation.**
120 Alternatively, pandemic perturbations can have a lasting impact on the forces driv-
121 ing pathogen dynamics through a long-term reduction in transmission or permanent
122 change in immunity. As an example, we consider a scenario in which a 10% reduc-
123 tion in transmission persists even after the major pandemic perturbations are lifted
124 (Figure 2D–F). In such cases, we cannot know whether the pathogen will return to
125 its original cycle or a different cycle until many years have passed, and we cannot
126 a priori measure the distance to the new unknown attractor that the system might
127 eventually approach. Nonetheless, we can still measure the distance from the pre-

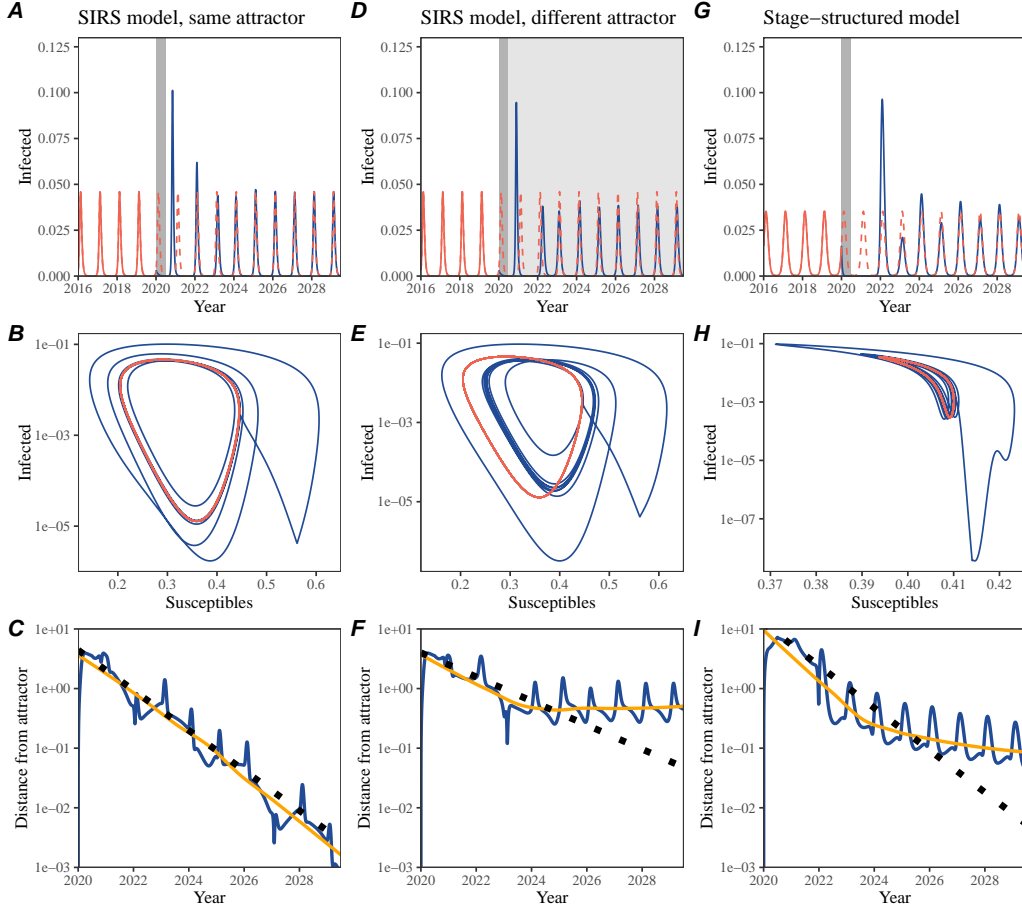


Figure 2: A simple method to measure pathogen resilience following pandemic perturbations across different scenarios. (A, D, G) Simulated epidemic trajectories across various models. Red and blue solid lines represent epidemic dynamics before and after pandemic perturbations are introduced, respectively. Red dashed lines represent counterfactual epidemic dynamics in the absence of perturbations. Gray regions indicate the duration of perturbations with the dark gray region representing a 50% transmission reduction and the light gray region representing a 10% transmission reduction. (B, E, H) Phase plane representation of the time series in panels A, D, and G alongside the corresponding susceptible host dynamics. Red and blue solid lines represent epidemic trajectories on an SI phase plane before and after perturbations are introduced, respectively. (C, F, I) Changes in distance from the attractor over time on a log scale. Blue lines represent the distance from the attractor. Orange lines represent the locally estimated scatterplot smoothing (LOESS) fits to the logged distance from the attractor. Dotted lines show the intrinsic resilience of the seasonally unforced system.

128 pandemic attractor and ask how the distance changes over time (Figure 2E). The
129 LOESS fit suggests that the distance from the pre-pandemic attractor will initially
130 decrease exponentially on average (equivalently, linearly on a log scale) and even-
131 tually plateau (Figure 2F). Here, a permanent 10% reduction in transmission rate
132 slows the system, which causes the distance from the pre-pandemic attractor initially
133 to decrease at a slower rate (Figure 2F) than it would have otherwise (Figure 2C)
134 before plateauing at a fixed distance between the two attractors. This example shows
135 that resilience is not necessarily an intrinsic property of a specific pathogen. Instead,
136 pathogen resilience is a property of a specific attractor that a host-pathogen system
137 approaches, which depends on both pathogen and host characteristics.

138 **Resilience of a single-strain system with long-term transients.** Finally,
139 transient phenomena can further complicate the picture (Figure 2G–I). For exam-
140 ple, a stage-structured model that accounts for reduction in secondary susceptibility
141 initially exhibits a stable annual cycle, but perturbations from a 10% reduction in
142 transmission for 6 months cause the epidemic to shift to biennial cycles (Figure 2G).
143 The system eventually approaches the original pre-pandemic attractor (Figure 2H),
144 suggesting that this biennial cycle is a transient. The LOESS fit indicates that the
145 distance from the attractor initially decreases exponentially at a rate that is consis-
146 tent with the intrinsic resilience of the seasonally unforced stage-structured system,
147 but the approach to the attractor slows down with the damped oscillations (Figure
148 2I). This behavior is also referred to as a ghost attractor, which causes long tran-
149 sient dynamics and slow transitions [20]. Strong seasonal forcing in transmission can
150 also lead to transient phenomena for a simple SIRS model, causing a slow return to
151 pre-perturbation dynamics (Supplementary Figure S1).

152 **Resilience of a two-strain system.** This empirical approach allows us to
153 measure the resilience of a two-strain host-pathogen system as well even when we
154 have incomplete observation of the infection dynamics. Simulations from a simple
155 two-strain competition system illustrate that separate analyses of individual strain
156 dynamics (e.g., RSV subtype A vs B) and a joint analysis of total infections (e.g.,
157 total RSV infections) yield identical resilience estimates (Supplementary Figure S2,
158 3). This is expected because eigenvalues determine the dynamics of the entire system
159 around the equilibrium, meaning that both strains should exhibit identical rates of
160 return following a perturbation. Analogous to a single-strain system, strong sea-
161 sonal forcing in transmission can cause the two-strain system to slow down through
162 transient phenomena (Supplementary Figure S4).

163 These observations yield three insights. First, we can directly estimate the empi-
164 rical resilience of a host-pathogen system by measuring the rate at which the system
165 approaches an attractor, provided that we have a way to quantify the distance from
166 the attractor—as we discuss later, the attractor of a system can be reconstructed
167 from data from mathematical theory without making assumptions about the under-
168 lying model. The empirical approach to estimating pathogen resilience is particularly
169 convenient because it does not require us to know the true underlying model; esti-
170 mating the intrinsic resilience from fitting misspecified models can lead to biased

estimates (Supplementary Figure S5). Second, resilience estimates allow us to make phenomenological predictions about the dynamics of a host-pathogen system following a perturbation. Assuming that an attractor has not changed and the distance from the attractor will decrease exponentially over time, we can estimate when the system should reach an attractor. Finally, a change in the (exponential) rate of approach can provide information about whether the system has reached an alternative attractor, or a ghost attractor, that is different from the original, pre-pandemic attractor. These alternative attractors may reflect permanent changes in transmission patterns as well as changes in immune landscapes. There will be periods of time when it is difficult to tell whether pathogen dynamics are still diverging from the original attractor due to a long-term perturbation, or have entered the basin of attraction of a new attractor. Now that several years have passed since major interventions have been lifted, many respiratory pathogens may have had sufficient time to begin returning to their post-intervention attractors—empirical comparisons between current cases and pre-pandemic cases are consistent with this hypothesis (Figure 1). With recent data, we can start to evaluate whether we see early signs of convergence to the former attractor or a new one.

Inferring pathogen resilience from real data

Based on these patterns, we now lay out our approach to estimating pathogen resilience from real data (Figure 3). We first tested this approach against simulations and applied it to real data. Specifically, we analyzed case time series of respiratory pathogens from four countries: Canada, Hong Kong, Korea, and the US.

So far, we have focused on simple examples that assume a constant transmission reduction during the pandemic. However, in practice, the impact of pandemic perturbations on pathogen transmission is likely more complex (Figure 3A), reflecting the introduction and relaxation of various intervention strategies. In some cases, strong perturbations likely caused local fadeouts, requiring immigration/importation from another location for epidemic rebound. Such complexities could lead to longer delays between the introduction of pandemic perturbations and pathogen rebound as well as temporal variation in outbreak sizes (Figure 3B); in this example, continued transmission reduction from interventions limits the size of the first outbreak in 2021 following the rebound, allowing for a larger outbreak in 2022 when interventions are further relaxed.

Previously, we relied on the dynamics of susceptible and infected hosts to compute the distance from the attractor (Figure 2), but information on susceptible hosts is rarely available in practice. In addition, uncertainties in case counts due to observation error, strain evolution, and multiannual cycles in the observed epidemic dynamics (e.g., adenovirus circulation patterns in Hong Kong and Korea) add challenges to defining pre-pandemic attractors, which limits our ability to measure the distance from the attractor. To address these challenges, we can reconstruct an em-

211 empirical attractor by utilizing Takens' theorem [17], which states that an attractor of a
212 nonlinear multidimensional system can be mapped onto a delayed embedding (Materials
213 and Methods). For example, we can use delayed logged values of pre-pandemic
214 cases $C(t)$ (Figure 3C) to reconstruct the attractor:

$$\langle \log(C(t) + 1), \log(C(t - \tau) + 1), \dots, \log(C(t - (M - 1)\tau) + 1) \rangle, \quad (1)$$

215 where the delay τ and embedding dimension M are determined based on autocor-
216 relations and false nearest neighbors, respectively [21, 22]. This allows us to define
217 the pre-pandemic attractor as a points on an M -dimensional space. We can then
218 apply the same delay and embedding dimensions to the entire time series to deter-
219 mine the position in multi-dimensional state space (Figure 3D), which allows us to
220 measure the nearest neighbor distance between the current state of the system and
221 the empirical pre-pandemic attractor (Figure 3E). Specifically, the nearest neighbor
222 distance is calculated by computing the distance between the current position on
223 the M -dimensional space and all points in the empirical attractor set and taking the
224 minimum value. In theory, we can now quantify how fast this distance decreases by
225 fitting a linear regression on a log scale, where the slope of the linear regression em-
226 pirically measures pathogen resilience, with a steeper slope corresponding to a higher
227 resilience estimate (Figure 3E). However, resulting estimates of pathogen resilience
228 can be sensitive to choices about embedding delays and dimensions. For example,
229 using longer delays and higher dimensions tends to smooth out temporal variations
230 in the distance from the attractor (Supplementary Figure S6).

231 Complex changes in the distance from the attractor suggest that estimating
232 pathogen resilience from linear regression will be particularly sensitive to our choice
233 of fitting windows for the regression (Figure 3E). Therefore, before we tried estimat-
234 ing resilience from real data, we explored an automated window selection criteria
235 for linear regression and tested it against randomized, stochastic simulations across
236 a range of realistic pandemic perturbation shapes. In doing so, we also explored
237 optimal choices for embedding dimensions and evaluated our choices of fitting win-
238 dows parameters and embedding dimensions by quantifying correlation coefficients
239 between the estimated resilience and the intrinsic resilience of a seasonally unforced
240 system (Materials and Methods). Overall, we found large variation in estimation
241 performances with correlation coefficients ranging from 0.21 to 0.61 (Supplementary
242 Figure S7). In almost all cases, the automated window selection approach outper-
243 formed a naive approach, which performs regression using all data from the the
244 timing of peak distance to current time (Supplementary Figure S7).

245 Based on the best-performing window selection criteria and embedding dimen-
246 sion, we applied this approach to pathogen surveillance data presented in Figure
247 1 (Materials and Methods). For each time series, we applied Takens' theorem in-
248 dependently to reconstruct the empirical attractor and obtained the corresponding
249 time series of distances from attractors (Supplementary Figure S8). Then, we used
250 the automated window selection criteria to fit a linear regression and estimated the
251 empirical resilience for each pathogen in each country (Supplementary Figure S8);

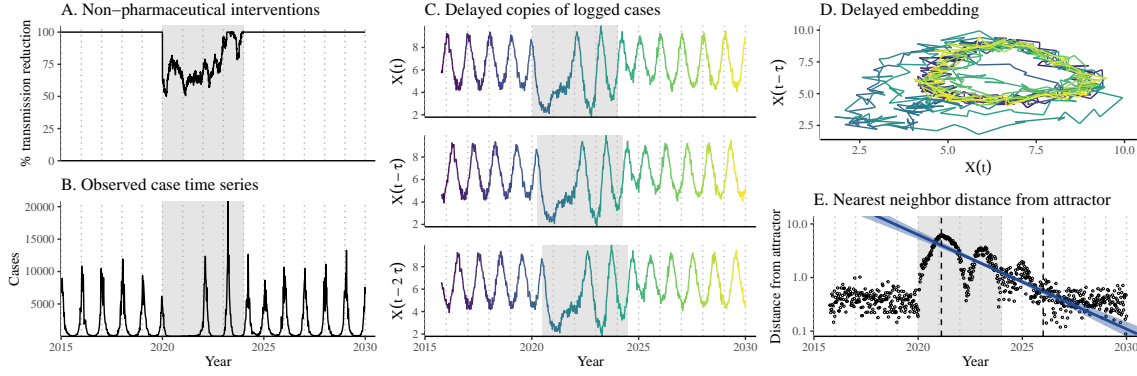


Figure 3: **A schematic diagram explaining the inference of pathogen resilience from synthetic data.** (A) A realistic example of simulated pandemic perturbations, represented by a relative reduction in transmission. (B) The impact of the synthetic pandemic perturbation on epidemic dynamics simulated using a SIRS model with demographic stochasticity. (C) Generating delayed copies of the logged time series allows us to obtain an embedding. (D) Two dimensional representation of an embedding. (E) Delayed embedding allows us to calculate the nearest neighbor distance from the empirical attractor, which is determined based on the pre-pandemic time series. Blue lines and dashed regions represent the linear regression fit and the associated 95% confidence interval. This distance time series can be used to infer pathogen resilience after choosing an appropriate window for linear regression. For illustration purposes, an arbitrary fitting window was chosen.

the window selection criteria gave poor regression windows in three cases (norovirus in Hong Kong and Korea and rhinovirus/enterovirus in the US), leading to unrealistically low resilience estimates, and so we used ad-hoc regression windows instead (Supplementary Figure S9; Materials and Methods).

For all pathogens we considered, resilience estimates fall between 0.4/year and 1.8/year (Figure 4A). We estimated the mean resilience of common respiratory pathogens to be 0.99/year (95% CI: 0.81/year–1.18/year). For reference, this is ≈ 7.5 times higher than the intrinsic resilience of pre-vaccination measles in England and Wales ($\approx 0.13/\text{year}$). Finally, resilience estimates for norovirus, a gastrointestinal pathogen, were comparable to those of common respiratory pathogens: 1.44/year (95% CI: 1.01/year–1.87/year) for Hong Kong and 1.07/year (95% CI: 0.86/year–1.29/year) for Korea. Based on a simple ANOVA test, we did not find significant differences in resilience estimates across countries ($p = 0.25$) or pathogens ($p = 0.67$).

Using resilience estimates, we predicted when each pathogen would hypothetically return to their pre-pandemic dynamics, assuming no long-term change in the attractor. Specifically, we extended our linear regression fits to distance-from-attractor time series and ask when the predicted regression line will cross a threshold value; since we relied on nearest neighbor distances, pre-pandemic distances are always greater than zero (Figure 3E), meaning that we can use the mean of pre-pandemic

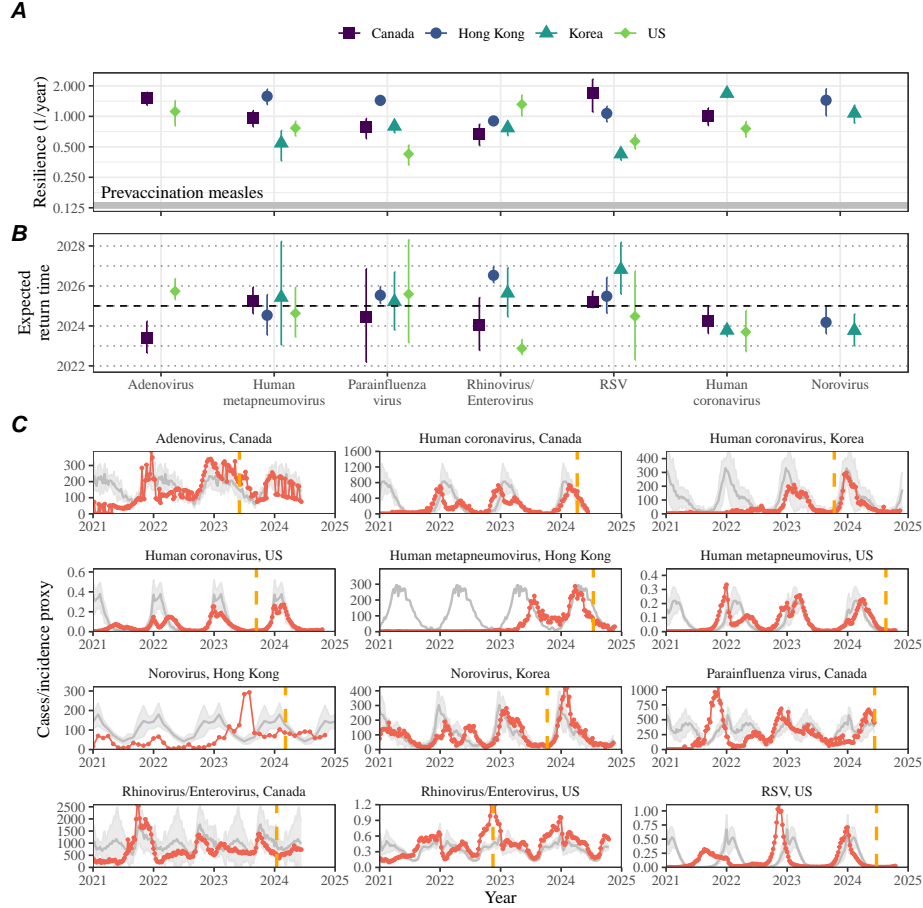


Figure 4: **Summary of resilience estimates and predictions for return time.** (A) Estimated pathogen resilience. The gray horizontal line represents the intrinsic resilience of pre-vaccination measles dynamics. (B) Predicted timing of when each pathogen will return to their pre-pandemic cycles. The dashed line in panel B indicates the end of 2024. Error bars represent 95% confidence intervals. (C) Observed dynamics for pathogen that are predicted to have returned before the end of 2024. Red points and lines represent data before 2020. Gray lines and shaded regions represent the mean seasonal patterns and corresponding 95% confidence intervals around the mean, previously shown in Figure 1. Orange vertical lines represent the predicted timing of return.

271 distances as our threshold.

272 We predicted that a return to pre-pandemic cycles has occurred or would be
 273 imminent for most pathogens (Figure 4B). In particular, we predicted that 12 out
 274 of 23 pathogen-country pairs should have already returned before the end of 2024.
 275 For almost all pathogens that were predicted to have returned already, the observed
 276 epidemic dynamics showed clear convergence towards their pre-pandemic seasonal

averages, confirming our predictions (Figure 4C). However, there were a few exceptions, including norovirus in Hong Kong and rhinovirus/enterovirus in the US, where the observed epidemic dynamics in 2024 exhibit clear deviation from their pre-pandemic seasonal averages (Figure 4C; Figure S9). These observations suggest a possibility that some common respiratory pathogens may have converged to different attractors or are still exhibiting non-equilibrium dynamics. In contrast, pathogens that were predicted to have not returned yet also showed clear differences from their pre-pandemic seasonal averages; as many of these pathogens are predicted to return in 2025–2026, we may be able to test these predictions in near future (Supplementary Figure S10). Our reconstructions of distance time series and estimates of pathogen resilience and expected return time were generally robust to choices of embedding dimensions (Supplementary Figure S11–12).

Susceptible host dynamics explain variation in pathogen resilience

So far, we have focused on quantifying pathogen resilience from the observed patterns of pathogen re-emergence following pandemic perturbations. But what factors determine the resilience of a host-pathogen system? To address this question, we used the SIRS model to explore how changes in susceptible host dynamics affect pathogen resilience. To do so, we varied the basic reproduction number \mathcal{R}_0 , which represents the average number of secondary infections caused by a newly infected individual in a fully susceptible population, and the duration of immunity and computed intrinsic resilience for each parameter.

We found that an increase in \mathcal{R}_0 and a decrease in the duration of immunity correspond to an increase in pathogen resilience (Figure 5A). Similarly, an increase in \mathcal{R}_0 and a decrease in the duration of immunity corresponds to a faster per-capita rate of susceptible replenishment, which is defined as the ratio between absolute rate at which new susceptibles enter the population and the equilibrium number of susceptible individuals in the population, S^* (Figure 5B). We note that a higher \mathcal{R}_0 drives a faster per-capita susceptible replenishment rate by decreasing the susceptible proportion at equilibrium, S^* . For a simple SIR model that assumes a life-long immunity, we can show analytically that pathogen resilience is proportional to the per-capita rate of susceptible replenishment (Materials and Methods). Overall, these observations suggest that a faster per-capita susceptible replenishment rate causes the system to be more resilient.

By taking the average values of empirical resilience for each pathogen, we were able to map each pathogen onto a set of parameters of the SIRS model that are consistent with corresponding resilience estimates (Figure 5A). Across all pathogens we considered, we estimated that the average duration of immunity is likely to be short (< 4 years) across a plausible range of \mathcal{R}_0 (< 6). We were also able to obtain a plausible range of susceptible replenishment rates for each pathogen (Figure 5B),

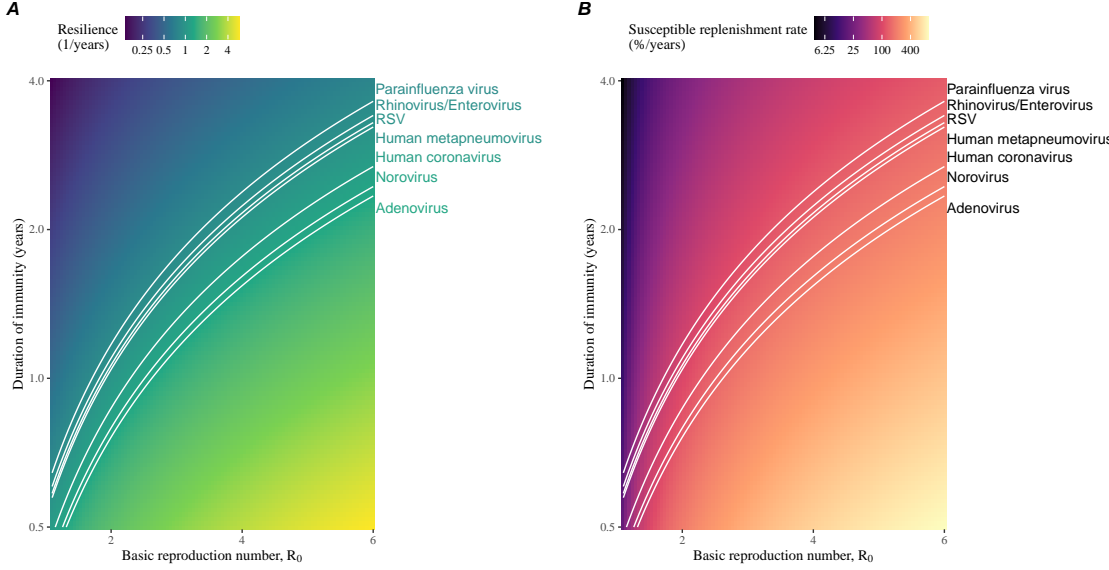


Figure 5: Linking pathogen resilience to epidemiological parameters and susceptible host dynamics. (A) Intrinsic resilience as a function of the basic reproduction number \mathcal{R}_0 and the duration of immunity. (B) Per-capita susceptible replenishment rate as a function of the basic reproduction number \mathcal{R}_0 and the duration of immunity. The standard SIRS model without seasonal forcing is used to compute intrinsic resilience and the per-capita susceptible replenishment rate. Lines correspond to a set of parameters that are consistent with mean resilience estimates for each pathogen, averaged across different countries.

317 but there was a large uncertainty in the estimates for susceptible replenishment rates
 318 due to a lack of one-to-one correspondence between susceptible replenishment rates
 319 and pathogen resilience.

320 Pathogen resilience determines sensitivity to stochastic perturbations

322 Even in the absence of major pandemic perturbations, host-pathogen systems are
 323 expected to experience continued perturbations of varying degrees from changes in
 324 epidemiological conditions, such as human behavior, climate, and viral evolution.
 325 These perturbations can also arise from demographic stochasticity, which is inher-
 326 ent to any ecological system. Here, we used a seasonally unforced SIRS model with
 327 constant birth and death rates to explore how resilience of a host-pathogen sys-
 328 tem determines the sensitivity to perturbations caused by demographic stochasticity
 329 (Materials and Methods).

330 We found that resilience of a host-pathogen system determines the amount of de-

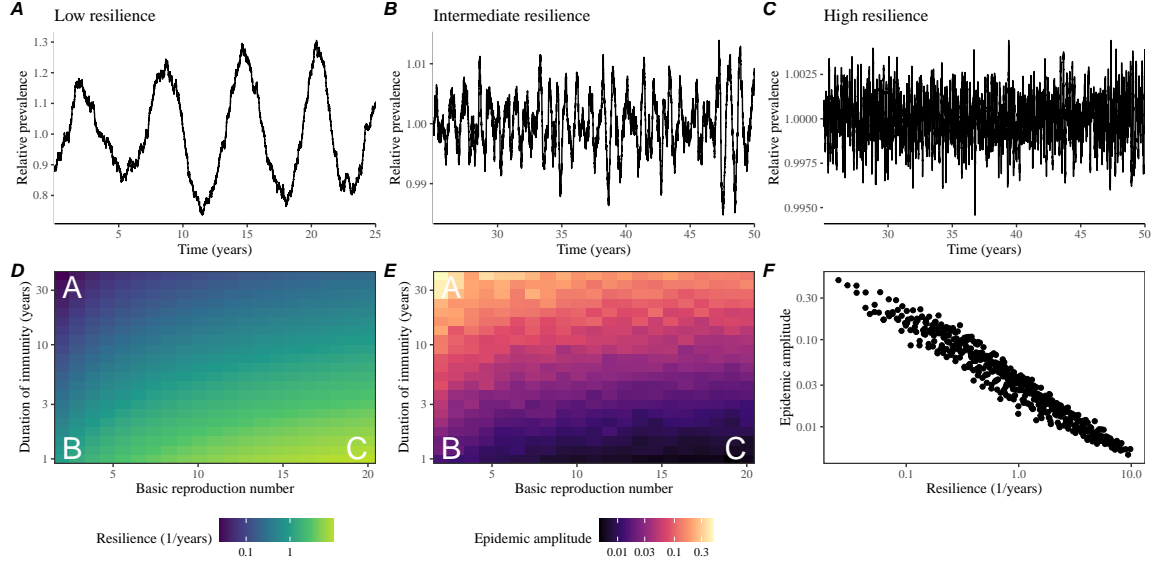


Figure 6: Linking resilience of a host-pathogen system to its sensitivity to stochastic perturbations. (A–C) Epidemic trajectories of a stochastic SIRS model across three different resilience values: low, intermediate, and high. The relative prevalence was calculated by dividing infection prevalence by its mean value. (D) Intrinsic resilience of a system as a function of the basic reproduction number \mathcal{R}_0 and the duration of immunity. (E) Epidemic amplitude as a function of the basic reproduction number \mathcal{R}_0 and the duration of immunity. The epidemic amplitude corresponds to $(\max I - \min I)/(2\bar{I})$, where \bar{I} represents the mean prevalence. Labels A–C in panels D and E correspond to scenarios shown in panels A–C. (F) The relationship between pathogen resilience and epidemic amplitude.

331 deviation from the deterministic trajectory caused by demographic stochasticity, with
 332 less resilient systems experiencing larger deviations (Figure 6). Notably, less resilient
 333 systems also exhibited slower epidemic cycles (Figure 6A–C). The periodicity of this
 334 epidemic cycle matched those predicted by the intrinsic periodicity of the system
 335 (Supplementary Figure S13) where the intrinsic resilience of the system is inversely
 336 proportional to its intrinsic periodicity (Supplementary Figure S14). However, we
 337 note that the interplay between seasonal transmission and intrinsic periodicity can
 338 also lead to complex cycles, as illustrated by a recent analysis of *Mycoplasma pneumoniae*
 339 dynamics [23].

340 We also note that the intrinsic resilience is not the sole determinant for how sen-
 341 sitive the system is to stochastic perturbations. For example, the population size
 342 and average duration of infection also affect the amount of deviation from the deter-
 343 ministic trajectory caused by demographic stochasticity, even though these quantities
 344 have little to no impact on the intrinsic resilience (Supplementary Figure S15). These
 345 conclusions were robust for the seasonally forced SIRS model (Supplementary Figure

346 S16).

347 Discussion

348 COVID-19 pandemic interventions caused major disruptions to circulation patterns
349 of both respiratory and non-respiratory pathogens, adding challenges to predicting
350 their future dynamics [1, 2, 3, 4]. However, these perturbations offer large-scale natu-
351 ral experiments for understanding how different pathogens respond to perturbations.
352 In this study, we showed that pathogen re-emergence patterns following pandemic
353 perturbations can be characterized through the lens of ecological resilience and pre-
354 sented a new method for estimating pathogen resilience from time series data. We
355 showed that variation in pathogen resilience can be explained by the differences in
356 susceptible host dynamics, where faster replenishment of the susceptible pool corre-
357 sponds to a more resilient host-pathogen system. Finally, we showed that pathogen
358 resilience also determines the sensitivity to stochastic perturbations.

359 We analyzed case time series of common respiratory infections and norovirus
360 infections from Canada, Hong Kong, Korea, and the US to estimate their resilience.
361 Overall, we estimated the resilience of these pathogens to range from 0.4/year to
362 1.8/year, which is 3–14 times more resilient than prevaccination measles. Consistent
363 with other epidemiological evidence [24, 25, 26, 27], these resilience estimates indicate
364 that common respiratory pathogens and norovirus likely exhibit faster susceptible
365 replenishment and are therefore more persistent, indicating potential challenges in
366 controlling these pathogens.

367 Based on our resilience estimates, we made phenomenological predictions about
368 when each pathogen will return to their endemic cycles. For the most part, we
369 accurately predicted which pathogens should have already returned before the end
370 of 2024. However, there were two main exceptions (i.e., norovirus in Hong Kong
371 and rhinovirus/enterovirus in the US), suggesting that these pathogens may be con-
372 verging to new endemic cycles or experiencing long-term transient behavior. These
373 changes may reflect changes in surveillance or actual shift in the dynamics, caused
374 by permanent changes in behavior or population-level immunity. While it may seem
375 unlikely that permanent changes in behavior would only affect a few pathogens and
376 not others, we cannot rule out this possibility given differences in the observed mean
377 age of infections and therefore the differences in age groups that primarily drive
378 transmission [28, 29]. Differences in the mode of transmission between respiratory
379 vs gastrointestinal pathogens may also contribute to the differences in responses to
380 pandemic perturbations.

381 For almost half of the pathogens we considered, we predicted that their return
382 to original epidemic patterns is imminent. We will need a few more years of data
383 to test whether these pathogens will eventually return to their original dynamics or
384 eventually converge to a different attractor. We also cannot rule out the possibility
385 that some pathogens may exhibit long-term transient behaviors following pandemic

386 perturbations. Overall, these observations echo earlier studies that highlighted the
387 long-lasting impact of pandemic perturbations [8, 30, 31, 4, 23].

388 We showed that susceptible host dynamics shape pathogen resilience, where faster
389 replenishment of the susceptible population causes the pathogen to be more resilient.
390 For simplicity, we focused on waning immunity and birth as the main drivers of the
391 susceptible host dynamics but other mechanisms can also contribute to the replen-
392 ishment of the susceptible population. In particular, pathogen evolution, especially
393 the emergence of antigenically novel strains, can cause effective waning of immunity
394 in the population; therefore, we hypothesize that the rate of antigenic evolution is
395 likely a key feature of pathogen resilience. Future studies should explore the relation-
396 ship between the rate of evolution and resilience for antigenically evolving pathogens.
397 This result also highlights the importance of detailed measurements of changes in the
398 susceptible population through immune assays for understanding pathogen dynamics
399 [32].

400 Quantifying pathogen resilience also offers novel approaches to validating population-
401 level epidemiological models. So far, most model validation in infectious disease ecol-
402 ogy is based on the ability of a model to reproduce the observed epidemic dynamics
403 and to predict future dynamics [33, 34, 26, 35, 36]. However, many models can
404 perform similarly under these criteria. For example, two major RSV models have
405 been proposed to explain biennial epidemic patterns: (1) a stage- and age-structured
406 model that allows disease severity to vary with number of past infections and age of
407 infection [26] and (2) a pathogen-interaction model that accounts for cross immunity
408 between RSV and human metapneumovirus [34]. Since both models can accurately
409 reproduce the observed epidemic patterns, standard criteria for model validation
410 do not allow us to distinguish between these two models from population-level data
411 alone. Instead, it would be possible to measure the empirical resilience of each model
412 by simulating various perturbations and comparing the simulations to estimates of
413 empirical resilience from data, using pandemic perturbations as a reference.

414 There are several limitations to our work. First, we did not extensively explore
415 other approaches to reconstructing the attractor. Recent studies showed that more
416 sophisticated approaches, such as using non-uniform embedding, can provide more
417 robust reconstruction for noisy data [22]. In the context of causal inference, choices
418 about embedding can have major impact on the resulting inference [37]. Our re-
419 silience estimates are likely overly confident given a lack of uncertainties in attractor
420 reconstruction as well as the simplicity of our statistical framework. Nonetheless,
421 as illustrated in our sensitivity analyses, inferences about pathogen resilience in our
422 SIRS model appear to be robust to decisions about embedding lags and dimensions—
423 this is because tracking the rate at which the system approaches the attractor is likely
424 a much simpler problem than making inferences about causal directionality. Short
425 pre-pandemic time series also limit our ability to accurately reconstruct the attrac-
426 tor and contribute to the crudeness of our resilience estimates; although this is less
427 likely a problem for respiratory pathogens that are strongly annual, our attractor
428 reconstruction may be inaccurate for those exhibiting multi-annual cycles, such as

429 adenovirus in Hong Kong and Korea. Our framework also does not allow us to dis-
430tinguish whether a system has settled to a new attractor or is experiencing long-term
431 transient behavior. Uncertainties in pathogen dynamics due to changes in testing
432 patterns further contribute to the crudeness of our resilience estimates.

433 While attractor reconstruction allows us to make model-free inferences of pathogen
434 resilience, it does not allow us to tease apart how different mechanisms contribute
435 to the resilience a host-pathogen system. Using the simple SIRS model, we illus-
436 trated that susceptible host dynamics are key determinants of pathogen resilience,
437 but we also found that there isn't a one-to-one correspondence between per capita
438 replenishment rate of the susceptible population and pathogen resilience estimates.
439 Future studies should explore using mechanistic models to explain heterogeneity in
440 resilience estimates across different pathogens.

441 Finally, our simulation-based analyses primarily focused on single-strain systems,
442 but real-world pathogens can interact with other pathogens, which can result in com-
443 plex dynamics [38, 39]. To address this limitation, we considered a simple model of
444 two competing strains (via cross immunity) and showed that the resilience of a cou-
445 pled system can be measured by studying the dynamics of either strain. However, this
446 conclusion likely depends on the strength and mechanism of strain interactions. For
447 example, ecological interference between two unrelated pathogens [38] will likely gen-
448 erate weaker coupling than cross-immunity between related pathogens; in the former
449 case, we do not necessarily expect two unrelated pathogens to have same resilience
450 despite their ecological interference. Some pathogen strains can also exhibit positive
451 interactions where infection by one strain can lead to an increased transmission of
452 another competing strain. For example, previous studies showed that an increased
453 dengue transmission through antibody-dependent enhancement can permit coexis-
454 tence and persistence of competing strains [40]; since pathogen transmissibility is a
455 major determinant of pathogen resilience, we tentatively hypothesize that positive
456 interactions such as antibody-dependent enhancement may increase the resilience of
457 a system. Future studies should explore how different mechanisms of pathogen inter-
458 actions contribute to the resilience of each competing pathogen as well as the entire
459 system. Despite these limitations, our study illustrates that quantifying pathogen
460 resilience can provide novel insights into pathogen dynamics. Furthermore, our qual-
461 itative prediction that common respiratory pathogens are more resilient than pre-
462 vaccination measles is also likely to be robust, given how rapidly many respiratory
463 pathogens returned to their original cycles following pandemic perturbations.

464 Predicting the impact of anthropogenic changes on infectious disease dynamics
465 is a fundamental aim of infectious disease research in a rapidly changing world. Our
466 study illustrates that how a host-pathogen system responds to both small and large
467 perturbations is largely predictable through the lens of ecological resilience. In par-
468 ticular, quantifying the resilience of a host-pathogen system offers a unique insight
469 into questions about endemic pathogens' responses to pandemic perturbations, in-
470 cluding whether some pathogens will exhibit long-lasting impact from the pandemic
471 perturbation or not. More broadly, a detailed understanding of the determinants of

472 pathogen resilience can provide deeper understanding of pathogen persistence.

473 Materials and Methods

474 Data

475 We gathered time series on respiratory infections from Canada, Hong Kong, Korea,
476 and United States (US). As a reference, we also included time series data on norovirus
477 infections when available. In contrast to respiratory pathogens, we hypothesized
478 gastrointestinal viruses, such as norovirus, to be differently affected by pandemic
479 perturbations.

480 Weekly time series of respiratory infection cases in Canada came from a publicly
481 available website by the Respiratory Virus Detection Surveillance System, which
482 collects data from select laboratories across Canada [41]. Weekly time series of
483 respiratory infection cases in Hong Kong came from a publicly available website
484 by the Centre for Health Protection, Department of Health [42, 43]. Weekly time
485 series of acute respiratory infection cases in Korea came from a publicly available
486 website by the Korea Disease Control and Prevention Agency [44]. Finally, weekly
487 time series of respiratory infection cases in the US were obtained from the National
488 Respiratory and Enteric Virus Surveillance System (NREVSS). Readers can request
489 the data from NREVSS at nrevss@cdc.gov. Time series on number of tests were also
490 available in Canada, Hong Kong, and the US, but not in Korea.

491 Data processing

492 For all time series, we rounded every year to 52 weeks by taking the average number
493 of cases and tests between the 52nd and 53rd week. We also rescaled all time series to
494 account for changes in testing patterns, which were then used for the actual analysis.

495 For Canada, an increase in testing was observed from 2013 to 2024 (Supplementary
496 Figure S17). To account for this increase, we calculated a 2 year moving average
497 for the number of tests for each pathogen, which we used as a proxy for testing effort.
498 Then, we divided the smoothed testing patterns by the smoothed value at the final
499 week such that the testing effort has a maximum of 1. We then divided weekly cases
500 by the testing effort to obtain a scaled case time series. A similar approach was used
501 earlier for an analysis of RSV time series in the US to account for changes in testing
502 patterns [26].

503 For Hong Kong, we applied the same scaling procedure to the time series as we
504 did for Canada. In this case, we only adjusted for testing efforts up to the end of 2019
505 because there was a major reduction in testing for common respiratory pathogens
506 between 2020 and 2023 (Supplementary Figure S18).

507 For Korea, while we did not have information on testing, the reported number
508 of respiratory infections consistently increased from 2013 to the end of 2019, which
509 we interpreted as changes in testing patterns (Supplementary Figure S19). Since

510 we did not have testing numbers, we used the weekly sum of all acute respiratory
511 viral infection cases as a proxy for testing, which were further smoothed with moving
512 average and scaled to have a maximum of 1. For Korea, we also only adjusted for
513 testing efforts up to the end of 2019.

514 In the US, there has been a large increase in testing for some respiratory pathogens,
515 especially RSV, which could not be corrected by simple scaling (Supplementary Fig-
516 ure S20). Instead, we derived an incidence proxy by multiplying the test positivity
517 with influenza-like illness positivity, which was taken from <https://gis.cdc.gov/grasp/fluvie...>. This method of estimating an inci-
518 dence proxy has been recently applied in the analysis of seasonal coronaviruses [7]
519 and *Mycoplasma pneumoniae* infections [4]. Detailed assumptions and justifications
520 are provided in [45].

522 Data summary

523 To make qualitative comparisons between pre- and post-perturbation dynamics of
524 respiratory pathogen circulation patterns, we calculated the mean seasonal patterns
525 using time series of either rescaled cases or incidence proxy estimates before 2020. We
526 did so by taking the mean value in each week across all years before 2020. Confidence
527 intervals around the means were calculated using a simple t test.

528 Estimating pathogen resilience

529 In order to measure pathogen resilience from surveillance data, we first reconstructed
530 the empirical pre-pandemic attractor of the system using Takens' embedding theorem
531 [17]. Specifically, for a given pathogen, we took the pre-pandemic (before 2020) case
532 time series $C(t)$ and reconstructed the attractor using delayed embedding with a
533 uniform delay of τ and dimension M :

$$X_{\tau,m}(t) = \langle \log(C(t) + 1), \log(C(t - \tau) + 1), \dots, \log(C(t - (M - 1)\tau) + 1) \rangle. \quad (2)$$

534 Here, the delay τ was determined by calculating the autocorrelation of the logged
535 pre-pandemic time series and asking when the autocorrelation crosses 0 for the first
536 time [22]; a typical delay for an annual outbreak is around 13 weeks.

537 Then, for a given delay τ , we determined the embedding dimension M using the
538 false nearest neighbors approach [21, 22]. To do so, we started with an embedding
539 dimension e and constructed a set of points $A_{\tau,e} = \{X_{\tau,e}(t) | t < 2020\}$. Then, for
540 each point $X_{\tau,e}(t)$, we determined the nearest neighbor from the set $A_{\tau,e}$, which we
541 denote $X_{\tau,e}(t_{nn})$ for $t \neq t_{nn}$. Then, if the distance between these two points in the
542 $e+1$ dimension, $D_{\tau,e+1}(t) = \|X_{\tau,e+1}(t_{nn}) - X_{\tau,e+1}(t)\|_2$, is larger than their distance in
543 the e dimension, $D_{\tau,e}(t) = \|X_{\tau,e}(t_{nn}) - X_{\tau,e}(t)\|_2$, these two points are deemed to be
544 false nearest neighbors; specifically, we used a threshold R for the ratio between two
545 distances $D_{\tau,e+1}(t)/D_{\tau,e}(t)$ to determine false nearest neighbors. The first embed-
546 ding dimension e that does not have any false nearest neighbors corresponds to the

547 embedding dimension M for a given pathogen-country pair. For the main analysis,
 548 we used $R = 10$, which was chosen from a sensitivity analysis against simulated data
 549 (Supplementary Text). Once we determined the embedding lag τ and dimension M ,
 550 we apply the embedding to the entire time series and calculate the nearest neighbor
 551 distance against the attractor $A_{\tau,M}$ to obtain a time series of distance from the
 552 attractor $D_{\tau,M}(t)$.

553 From a time series of distances from the attractor, we estimated pathogen resilience
 554 by fitting a linear regression to an appropriate window. To automatically
 555 select fitting windows, we began by smoothing the distance time series using locally
 556 estimated scatterplot smoothing (LOESS) to obtain $\hat{D}_{\tau,M}(t)$, where the smoothing
 557 is performed on a log scale and exponentiated afterwards. This smoothing allowed
 558 us to find appropriate threshold values for selecting fitting windows that are insensitive
 559 to errors in our estimates of distance from the attractor. Then, we determined
 560 threshold values (T_{start} and T_{end}) for the smoothed distances and choose the fitting
 561 window based on when $\hat{D}_{\tau,M}(t)$ crosses these threshold values for the first time.
 562 These thresholds were determined by first calculating the maximum distance,

$$\max \hat{D} = \max \hat{D}_{\tau,M}(t), \quad (3)$$

563 and the mean pre-pandemic distance,

$$\hat{D}_{\text{mean}} = \frac{1}{N_{t < 2020}} \sum_{t < 2020} \hat{D}_{\tau,M}(t), \quad (4)$$

564 as a reference, and then dividing their ratios into K equal bins,

$$T_{\text{start}} = \hat{D}_{\text{mean}} \times \left(\frac{\max \hat{D}}{\hat{D}_{\text{mean}}} \right)^{(K-a)/K}, \quad (5)$$

$$T_{\text{end}} = \hat{D}_{\text{mean}} \times \left(\frac{\max \hat{D}}{\hat{D}_{\text{mean}}} \right)^{a/K}, \quad (6)$$

565 where a represents the truncation threshold. This allows us to discard the initial
 566 period during which the distance increases (from the introduction of intervention
 567 measures) and the final period during which the distance plateaus (as the system
 568 reaches an attractor). The fitting window is determined based on when the smoothed
 569 distance $\hat{D}_{\tau,M}(t)$ crosses these threshold values for the first time; then, we fit a
 570 linear regression to logged (unsmoothed) distances $\log D_{\tau,M}(t)$ using that window.
 571 Alongside the threshold R for the false nearest neighbors approach, we tested optimal
 572 choices for K and a values using simulations (Supplementary Text). We used $K = 19$
 573 and $a = 2$ throughout the paper based on the simulation results.

574 Mathematical modeling

575 Throughout the paper, we use a series of mathematical models to illustrate the
 576 concept of pathogen resilience and to understand the determinants of pathogen re-

577 silience. In general, the intrinsic resilience of a given system is given by the largest
 578 real part of the eigenvalues of the linearized system at endemic equilibrium. Here, we
 579 focus on the SIRS model with demography (birth and death) and present the details
 580 of other models in Supplementary Text. The SIRS (Susceptible-Infected-Recovered-
 581 Susceptible) model is the simplest model that allows for waning of immunity, where
 582 recovered (immune) individuals are assumed to become fully susceptible after an
 583 average of $1/\delta$ time period. The dynamics of the SIRS model is described by the
 584 following set of differential equations:

$$\frac{dS}{dt} = \mu - \beta(t)SI - \mu S + \delta R \quad (7)$$

$$\frac{dI}{dt} = \beta(t)SI - (\gamma + \mu)I \quad (8)$$

$$\frac{dR}{dt} = \gamma I - (\delta + \mu)R \quad (9)$$

585 where μ represents the birth and death rates, $\beta(t)$ represents the time-varying trans-
 586 mission rate, and γ represents the recovery rate. The basic reproduction number
 587 $\mathcal{R}_0(t) = \beta(t)/(\gamma + \mu)$ is defined as the average number of secondary infections that
 588 a single infected individual would cause in a fully susceptible population at time t
 589 and measures the intrinsic transmissibility of a pathogen.

590 When we introduced the idea of pathogen resilience (Figure 2), we imposed sinu-
 591 soidal changes to the transmission rate to account for seasonal transmission,

$$\beta(t) = b_1(1 + \theta \cos(2\pi(t - \phi)))\alpha(t), \quad (10)$$

592 where b_1 represents the baseline transmission rate, θ represents the seasonal ampli-
 593 tude, and ϕ represents the seasonal offset term. Here, we also introduced an extra
 594 multiplicative term $\alpha(t)$ to account for the impact of pandemic perturbations, where
 595 $\alpha(t) < 1$ indicates transmission reduction. Figure 2A and 2B were generated assum-
 596 ing $b_1 = 3 \times (365/7 + 1/50)/\text{years}$, $\theta = 0.2$, $\phi = 0$, $\mu = 1/50/\text{years}$, $\gamma = 365/7/\text{years}$,
 597 and $\delta = 1/2/\text{years}$. Specifically, $b_1 = 3 \times (365/7 + 1/50)/\text{years}$ implies $\mathcal{R}_0 = 3$, where
 598 $(365/7 + 1/50)/\text{years}$ represent the rate of recovery. In Figure 2A, we imposed a 50%
 599 transmission reduction for 6 months from 2020:

$$\alpha(t) = \begin{cases} 0.5 & 2020 \leq t < 2020.5 \\ 1 & \text{otherwise} \end{cases} \quad (11)$$

600 In Figure 2B, we imposed a 50% transmission reduction for 6 months from 2020 and
 601 a permanent 10% reduction onward:

$$\alpha(t) = \begin{cases} 1 & t < 2020 \\ 0.5 & 2020 \leq t < 2020.5 \\ 0.9 & 2020.5 \leq t \end{cases} \quad (12)$$

602 In both scenarios, we simulated the SIRS model from the same initial conditions
 603 ($S(0) = 1/\mathcal{R}_0$, $I(0) = 1 \times 10^{-6}$, and $R(0) = 1 - S(0) - I(0)$) from 1900 until 2030.
 604 Throughout the paper, all deterministic models were solved using the `lsoda` solver
 605 from the `deSolve` package [46] in R [47].

606 To measure the empirical resilience of the SIRS model (Figure 2C and 2F), we
 607 computed the normalized distance between post-intervention susceptible and logged
 608 infected proportions and their corresponding unperturbed values at the same time:

$$\sqrt{\left(\frac{S(t) - S_{\text{unperturbed}}(t)}{\sigma_S}\right)^2 + \left(\frac{\log I(t) - \log I_{\text{unperturbed}}(t)}{\sigma_{\log I}}\right)^2}, \quad (13)$$

609 where σ_S and $\sigma_{\log I}$ represent the standard deviation in the unperturbed susceptible
 610 and logged infected proportions. The unperturbed values were obtained by simulating
 611 the same SIRS model without pandemic perturbations ($\alpha = 1$). We normalized
 612 the differences in susceptible and logged infected proportions to allow both quantities
 613 to equally contribute to the changes in distance from the attractor. We used logged
 614 prevalence, instead of absolute prevalence, in order to capture epidemic dynamics
 615 in deep troughs during the intervention period. In Supplementary Materials, we
 616 also compared how the degree of seasonal transmission affects empirical resilience
 617 by varying θ from 0 to 0.4; when we assumed no seasonality ($\theta = 0$), we did not
 618 normalize the distance because the standard deviation of pre-intervention dynamics
 619 are zero.

620 We used the SIRS model to understand how underlying epidemiological parameters
 621 affect pathogen resilience and determine the relationship to underlying susceptible host dynamics. For the simple SIRS model without seasonal transmission
 622 ($\theta = 0$), the intrinsic resilience equals

$$-\frac{\text{Re}(\lambda)}{2} = \frac{\delta + \beta I^* + \mu}{2}. \quad (14)$$

624 Here, I^* represents the prevalence at endemic equilibrium:

$$I^* = \frac{(\delta + \mu)(\beta - (\gamma + \mu))}{\beta(\delta + \gamma + \mu)}. \quad (15)$$

625 The susceptible replenishment rate is given by

$$S_{\text{replenish}} = \frac{\mu + \delta R}{S^*}, \quad (16)$$

626 where $S^* = 1/\mathcal{R}_0$ represents the equilibrium proportion of susceptible individuals.
 627 We varied the basic reproduction number \mathcal{R}_0 between 1.1 to 6 and the average
 628 duration of immunity $1/\delta$ between 2 to 4 years, and computed these two quantities.
 629 In doing so, we fixed all other parameters: $\mu = 1/80/\text{years}$ and $\gamma = 365/7/\text{years}$.
 630 When infection provides a life-long immunity ($\delta = 0$), the intrinsic resilience is
 631 inversely proportional to the susceptible replenishment rate:

$$-\frac{\text{Re}(\lambda)}{2} = \frac{\mu}{2S^*} = \frac{S_{\text{replenish}}}{2}. \quad (17)$$

632 Finally, we used a seasonally unforced stochastic SIRS model without demog-
633 raphy to understand how pathogen resilience affects sensitivity of the system to
634 demographic stochasticity (see Supplementary Text for the details of the stochas-
635 tic SIRS model). By varying the basic reproduction number \mathcal{R}_0 between 2 to 20
636 and the average duration of immunity $1/\delta$ between 1 to 40 years, we ran the SIRS
637 model for 100 years and computed the epidemic amplitude, which we defined as
638 $(\max I - \min I)/(2\bar{I})$. Each simulation began from the equilibrium, and we trun-
639 cated the initial 25 years before computing the epidemic amplitude. In doing so,
640 we assumed $\gamma = 365/7/\text{years}$ and fixed the population size to 1 billion to prevent
641 any fadeouts. We also considered a seasonally forced stochastic SIRS model without
642 demography, assuming an amplitude of seasonal forcing of 0.04; in this case, we com-
643 puted the relative epidemic amplitude by comparing the deterministic and stochastic
644 trajectories (Supplementary Materials).

645 Acknowledgement

646 We thank Centers for Disease Control and Prevention, National Respiratory and
647 Enteric Virus Surveillance System (NREVSS) for providing time series data for res-
648 piratory infection cases in the US.

649 Data availability

650 All data and code are stored in a publicly available GitHub repository (<https://github.com/cobeylab/return-time>).

652 Funding

653 S.W.P. is a Peter and Carmen Lucia Buck Foundation Awardee of the Life Sciences
654 Research Foundation. B.F.N. acknowledges financial support from the Carlsberg
655 Foundation (grant no. CF23-0173). B.T.G is supported by Princeton Catalysis Ini-
656 tiative and Princeton Precision Health. S.C. is supported by Federal funds from the
657 National Institute of Allergy and Infectious Diseases, National Institutes of Health,
658 Department of Health and Human Services under CEIRR contract 75N93021C00015.
659 The content is solely the responsibility of the authors and does not necessarily repre-
660 sent the official views of the NIAID or the National Institutes of Health. This project
661 has been funded in whole or in part with Federal funds from the National Cancer In-
662 stitute, National Institutes of Health, under Prime Contract No. 75N91019D00024,
663 Task Order No. 75N91023F00016 (B.F.N., E.H., and B.T.G). The content of this
664 publication does not necessarily reflect the views or policies of the Department of
665 Health and Human Services, nor does mention of trade names, commercial products
666 or organizations imply endorsement by the U.S. Government.

667 **Supplementary Text**

668 **Resilience of a stage-structured system.**

669 In Figure 2G–I, we used a more realistic, stage-structured model to illustrate how
 670 transient phenomena can cause the system to slow down. Specifically, we used the
 671 stage-structured RSV model proposed by [26], which assumes that subsequent rein-
 672 fections cause an individual to become less susceptible and transmissible than previ-
 673 ous infections. In contrast to a standard SIRS model, this model does not include a
 674 recovered compartment, which allow for temporary protection against new infections,
 675 and assumes that recovered individuals are immediately susceptible to new infections.
 676 The model dynamics can be described as follows:

$$\frac{dM}{dt} = \mu - (\omega + \mu)M \quad (S1)$$

$$\frac{dS_0}{dt} = \omega M - (\lambda(t) + \mu)S_0 \quad (S2)$$

$$\frac{dI_1}{dt} = \lambda(t)S_0 - (\gamma_1 + \mu)I_1 \quad (S3)$$

$$\frac{dS_1}{dt} = \gamma_1 I_1 - (\sigma_1 \lambda(t) + \mu)S_1 \quad (S4)$$

$$\frac{dI_2}{dt} = \sigma_1 \lambda(t)S_1 - (\gamma_2 + \mu)I_2 \quad (S5)$$

$$\frac{dS_2}{dt} = \gamma_2 I_2 - (\sigma_2 \lambda(t) + \mu)S_2 \quad (S6)$$

$$\frac{dI_3}{dt} = \sigma_2 \lambda(t)S_2 - (\gamma_3 + \mu)I_3 \quad (S7)$$

$$\frac{dS_3}{dt} = \gamma_3 I_3 - (\sigma_3 \lambda(t) + \mu)S_3 + \gamma_4 I_4 \quad (S8)$$

$$\frac{dI_4}{dt} = \sigma_3 \lambda(t)S_3 - (\gamma_4 + \mu)I_4 \quad (S9)$$

677 where M represents the proportion of individuals who are maternally immune; S_i
 678 represents the proportion of individuals who are susceptible after i prior infections; I_i
 679 represents the proportion of individuals who are currently (re)-infected with their i -th
 680 infection; μ represents the birth and death rates; $1/\omega$ represents the mean duration
 681 of maternal immunity; $1/\gamma_i$ represents the mean duration of infection; $\lambda(t)$ represents
 682 the force of infection; and σ_i represents the reduction in susceptibility for the i -th
 683 reinfection. The force of infection is modeled using a sinusoidal function:

$$\beta(t) = b_1(1 + \theta \cos(2\pi(t - \phi)))\alpha(t) \quad (S10)$$

$$\lambda(t) = \beta(I_1 + \rho_1 I_2 + \rho_2(I_3 + I_4)), \quad (S11)$$

684 where b_1 represents the baseline transmission rate; θ represents the seasonal ampli-
 685 tude; ϕ represents the seasonal offset term; $\alpha(t)$ represents the intervention effect;

and ρ_i represents the impact of immunity on transmission reduction. We used the following parameters to simulate the impact of interventions on epidemic dynamics [26]: $b_1 = 9 \times (365/10 + 1/80)/\text{years}$, $\theta = 0.2$, $\phi = -0.1$, $\omega = 365/112/\text{years}$, $\gamma_1 = 365/10/\text{years}$, $\gamma_2 = 365/7/\text{years}$, $\gamma_3 = 365/5/\text{years}$, $\sigma_1 = 0.76$, $\sigma_2 = 0.6$, $\sigma_3 = 0.4$, $\rho_1 = 0.75$, $\rho_2 = 0.51$, and $\mu = 1/80/\text{years}$. We assumed a 50% transmission reduction for 6 months from 2020:

$$\alpha(t) = \begin{cases} 0.5 & 2020 \leq t < 2020.5 \\ 1 & \text{otherwise} \end{cases} \quad (\text{S12})$$

The model was simulated from 1900 to 2030 using the following initial conditions: $M = 0$, $S_0 = 1/\mathcal{R}_0 - I_1$, $I_1 = 1 \times 10^{-6}$, $S_1 = 1 - 1/\mathcal{R}_0$, $I_2 = 0$, $S_2 = 0$, $I_3 = 0$, $S_3 = 0$, and $I_4 = 0$. For the phase plane analysis (Figure 2H) and distance analysis (Figure 2I), we relied on the average susceptibility,

$$\bar{S} = S_0 + \sigma_1 S_1 + \sigma_2 S_2 + \sigma_3 S_3, \quad (\text{S13})$$

and total prevalence,

$$I_{\text{total}} = I_1 + I_2 + I_3 + I_4. \quad (\text{S14})$$

These quantities were used to compute the normalized distance from the attractor, as described in the main text.

We note that this system, without seasonally forced transmission rates, has 9 eigenvalues: -73.01, -53.11, -38.90, -3.27, $-0.82+2.57i$, $-0.82-2.57i$, -1.61, -1.18, and -0.01 (in the unit of 1/years). While the eigenvalue -0.01 has the largest real part, the magnitude is too close to 0 for the impact of this eigenvalue to be reflected in our resilience estimates. Instead, we chose real parts of the eigenvalues $-0.82 \pm 2.57i$ as our intrinsic resilience for this system and plotted them in Figure 2I; as we can see in this figure, this value captures the return rate of the system to the attractor.

Resilience of a multistrain system.

We used a simple two-strain model to show that a multistrain host-pathogen system that is coupled through cross immunity can be described by a single resilience value. The model dynamics can be described as follows [34]:

$$\frac{dS}{dt} = \mu - \mu S - (\lambda_1 + \lambda_2)S + \delta_1 R_1 + \delta_2 R_2 \quad (\text{S15})$$

$$\frac{dI_1}{dt} = \lambda_1 S - (\gamma_1 + \mu)I_1 \quad (\text{S16})$$

$$\frac{dI_2}{dt} = \lambda_2 S - (\gamma_2 + \mu)I_2 \quad (\text{S17})$$

$$\frac{dR_1}{dt} = \gamma_1 I_1 - \lambda_2 \epsilon_{21} R_1 - \delta_1 R_1 + \delta_2 R - \mu R_1 \quad (\text{S18})$$

$$\frac{dR_2}{dt} = \gamma_2 I_2 - \lambda_1 \epsilon_{12} R_2 - \delta_2 R_2 + \delta_1 R - \mu R_2 \quad (\text{S19})$$

$$\frac{dJ_1}{dt} = \lambda_1 \epsilon_{12} R_2 - (\gamma_1 + \mu) J_1 \quad (S20)$$

$$\frac{dJ_2}{dt} = \lambda_2 \epsilon_{21} R_1 - (\gamma_2 + \mu) J_2 \quad (S21)$$

$$\frac{dR}{dt} = \gamma_1 J_1 + \gamma_2 J_2 - \delta_1 R - \delta_2 R - \mu R \quad (S22)$$

where S represents the proportion of individuals who are fully susceptible to infections by both strains; I_1 represents the proportion of individuals who are infected with strain 1 without prior immunity; I_2 represents the proportion of individuals who are infected with strain 2 without prior immunity; R_1 represents the proportion of individuals who are fully immune against strain 1 and partially susceptible to reinfection by strain 2; R_2 represents the proportion of individuals who are fully immune against strain 2 and partially susceptible to reinfection by strain 1; J_1 represents the proportion of individuals who are infected with strain 1 with prior immunity against strain 2; J_2 represents the proportion of individuals who are infected with strain 2 with prior immunity against strain 1; R represents the proportion of individuals who are immune to infections from both strains; μ represents the birth/death rate; λ_1 and λ_2 represent the force of infection from strains 1 and 2, respectively; δ_1 and δ_2 represent the waning immunity rate; γ_1 and γ_2 represent the recovery rate; ϵ_{21} and ϵ_{12} represent the susceptibility to reinfection with strains 2 and 1, respectively, given prior immunity from infection with strains 1 and 2, respectively. The force of infection is modeled as follows:

$$\beta_1 = b_1(1 + \theta_1 \sin(2\pi(t - \phi_1)))\alpha(t) \quad (S23)$$

$$\beta_2 = b_2(1 + \theta_2 \sin(2\pi(t - \phi_2)))\alpha(t) \quad (S24)$$

$$\lambda_1 = \beta_1(I_1 + J_1) \quad (S25)$$

$$\lambda_2 = \beta_2(I_2 + J_2) \quad (S26)$$

In Supplementary Figures S2–S4, we assumed the following parameters: $b_1 = 2 \times 52/\text{years}$, $b_2 = 4 \times 52/\text{years}$, $\phi_1 = \phi_2 = 0$, $\epsilon_{12} = 0.9$, $\epsilon_{21} = 0.5$, $\gamma_1 = \gamma_2 = 52/\text{years}$, $\delta_1 = \delta_2 = 1/\text{years}$, and $\mu = 1/70/\text{years}$. For all simulations, we assumed a 50% transmission reduction for 6 months from 2020:

$$\alpha(t) = \begin{cases} 0.5 & 2020 \leq t < 2020.5 \\ 1 & \text{otherwise} \end{cases} \quad (S27)$$

The seasonal amplitude θ is varied from 0 to 0.4. All simulations were run from 1900 to 2030 with following initial conditions: $S(0) = 1 - 2 \times 10^{-6}$, $I_1(0) = 1 \times 10^{-6}$, $I_2(0) = 1 \times 10^{-6}$, $R_1(0) = 0$, $R_2(0) = 0$, $J_1(0) = 0$, $J_2(0) = 0$, and $R(0) = 0$.

We considered three scenarios for measuring pathogen resilience: (1) we only have information about strain 1, (2) we only have information about strain 2, and (3) we are unable to distinguish between strains. In the first two scenarios (see panels A–C for strain 1 and panels D–F for strain 2), we considered the dynamics of average

⁷³⁷ susceptibility for each strain and total prevalence:

$$\bar{S}_1 = S + \epsilon_{12}R_2 \quad (\text{S28})$$

$$\hat{I}_1 = I_1 + J_1 \quad (\text{S29})$$

$$\bar{S}_2 = S + \epsilon_{21}R_1 \quad (\text{S30})$$

$$\hat{I}_2 = I_2 + J_2 \quad (\text{S31})$$

⁷³⁸ In the third scenario (panels G–I), we considered the dynamics of total susceptible
⁷³⁹ and infected populations:

$$\hat{S} = S + R_2 + R_1 \quad (\text{S32})$$

$$\hat{I} = I_1 + J_1 + I_2 + J_2 \quad (\text{S33})$$

⁷⁴⁰ These quantities were used to compute the normalized distance from the attractor,
⁷⁴¹ as described in the main text.

⁷⁴² Estimating intrinsic resilience using a mechanistic model

⁷⁴³ We tested whether we can reliably estimate the intrinsic resilience of a system by fit-
⁷⁴⁴ ting a mechanistic model. Specifically, we simulated case time series from stochastic
⁷⁴⁵ SIRS and two-strain models and fitted a simple, deterministic SIRS model using a
⁷⁴⁶ Bayesian framework [4, 23, 48].

⁷⁴⁷ We simulated the models in discrete time with a daily time step ($\Delta t = 1$),
⁷⁴⁸ incorporating demographic stochasticity:

$$\beta(t) = \mathcal{R}_0 \left(1 + \theta \cos \left(\frac{2\pi t}{364} \right) \right) \alpha(t)(1 - \exp(-\gamma)) \quad (\text{S34})$$

$$\text{FOI}(t) = \beta(t)I(t - \Delta t)/N \quad (\text{S35})$$

$$B(t) \sim \text{Poisson}(\mu N) \quad (\text{S36})$$

$$\Delta S(t) \sim \text{Binom}(S(t - \Delta t), 1 - \exp(-(\text{FOI}(t) + \mu)\Delta t)) \quad (\text{S37})$$

$$N_{SI}(t) \sim \text{Binom}\left(\Delta S(t), \frac{\text{FOI}(t)}{\text{FOI}(t) + \mu}\right) \quad (\text{S38})$$

$$\Delta I(t) \sim \text{Binom}(I(t - \Delta t), 1 - \exp(-(\gamma + \mu)\Delta t)) \quad (\text{S39})$$

$$N_{IR}(t) \sim \text{Binom}\left(\Delta I(t), \frac{\gamma}{\gamma + \mu}\right) \quad (\text{S40})$$

$$\Delta R(t) \sim \text{Binom}(R(t - \Delta t), 1 - \exp(-(\delta + \mu)\Delta t)) \quad (\text{S41})$$

$$N_{RS}(t) \sim \text{Binom}\left(\Delta R(t), \frac{\delta}{\delta + \mu}\right) \quad (\text{S42})$$

$$S(t) = S(t - \Delta t) + N_{RS}(t) + B(t) - \Delta S(t) \quad (\text{S43})$$

$$I(t) = I(t - \Delta t) + N_{SI}(t) - \Delta I(t) \quad (\text{S44})$$

$$R(t) = R(t - \Delta t) + N_{IR}(t) - \Delta R(t) \quad (\text{S45})$$

where FOI represents the force of infection; N_{ij} represents the number of individuals moving from compartment i to j on a given day; and $B(t)$ represents the number of new births. All other parameters definitions can be found in the description of the deterministic version of the model. We simulated the model on a daily scale—assuming 364 days in a year so that it can be evenly grouped into 52 weeks—with the following parameters: $\mathcal{R}_0 = 3$, $\theta = 0.1$, $\gamma = 1/7/\text{days}$, $\delta = 1/(364 \times 2)/\text{days}$, $\mu = 1/(364 \times 50)/\text{days}$, and $N = 1 \times 10^8$. The model was simulated from 1900 to 2030 assuming $S(0) = N/3$, $I(0) = 100$, and $R(0) = N - S(0) - I(0)$. The observed incidence from the model was then simulated as follows:

$$C(t) = \text{Beta-Binom}(N_{SI}(t), \rho, k), \quad (\text{S46})$$

where ρ represents the reporting probability and k represents the overdispersion parameter of beta-binomial distribution. Here, we used the beta-binomial distribution to account for overdispersion in reporting. We assumed $\rho = 0.002$ (i.e., 0.2% probability) and $k = 1000$.

We used an analogous approach for the two-strain model:

$$\beta_1(t) = b_1 \left(1 + \theta_1 \cos \left(\frac{2\pi(t - \phi_1)}{364} \right) \right) \alpha(t) \quad (\text{S47})$$

$$\beta_2(t) = b_2 \left(1 + \theta_2 \cos \left(\frac{2\pi(t - \phi_2)}{364} \right) \right) \alpha(t) \quad (\text{S48})$$

$$\text{FOI}_1(t) = \beta_1(t)(I_1(t - \Delta t) + J_1(t - \Delta t))/N \quad (\text{S49})$$

$$\text{FOI}_2(t) = \beta_2(t)(I_2(t - \Delta t) + J_2(t - \Delta t))/N \quad (\text{S50})$$

$$B(t) \sim \text{Poisson}(\mu N) \quad (\text{S51})$$

$$\Delta S(t) \sim \text{Binom}(S(t - \Delta t), 1 - \exp(-(\text{FOI}_1(t) + \text{FOI}_2(t) + \mu)\Delta t)) \quad (\text{S52})$$

$$N_{SI_1}(t) \sim \text{Binom}\left(\Delta S(t), \frac{\text{FOI}_1(t)}{\text{FOI}_1(t) + \text{FOI}_2(t) + \mu}\right) \quad (\text{S53})$$

$$N_{SI_2}(t) \sim \text{Binom}\left(\Delta S(t), \frac{\text{FOI}_2(t)}{\text{FOI}_1(t) + \text{FOI}_2(t) + \mu}\right) \quad (\text{S54})$$

$$\Delta I_1(t) \sim \text{Binom}(I_1(t - \Delta t), 1 - \exp(-(\gamma_1 + \mu)\Delta t)) \quad (\text{S55})$$

$$N_{I_1 R_1}(t) \sim \text{Binom}\left(\Delta I_1(t), \frac{\gamma_1}{\gamma_1 + \mu}\right) \quad (\text{S56})$$

$$\Delta I_2(t) \sim \text{Binom}(I_2(t - \Delta t), 1 - \exp(-(\gamma_2 + \mu)\Delta t)) \quad (\text{S57})$$

$$N_{I_2 R_2}(t) \sim \text{Binom}\left(\Delta I_2(t), \frac{\gamma_2}{\gamma_2 + \mu}\right) \quad (\text{S58})$$

$$\Delta R_1(t) \sim \text{Binom}(R_1(t - \Delta t), 1 - \exp(-(\epsilon_{21}\text{FOI}_2(t) + \rho_1 + \mu)\Delta t)) \quad (\text{S59})$$

$$N_{R_1 S}(t) \sim \text{Binom}\left(\Delta R_1(t), \frac{\rho_1}{\epsilon_{21}\text{FOI}_2(t) + \rho_1 + \mu}\right) \quad (\text{S60})$$

$$N_{R_1 J_2}(t) \sim \text{Binom}\left(\Delta R_1(t), \frac{\epsilon_{21}\text{FOI}_2(t)}{\epsilon_{21}\text{FOI}_2(t) + \rho_1 + \mu}\right) \quad (\text{S61})$$

$$\Delta R_2(t) \sim \text{Binom}(R_2(t - \Delta t), 1 - \exp(-(\epsilon_{12}\text{FOI}_1(t) + \rho_2 + \mu)\Delta t)) \quad (\text{S62})$$

$$N_{R_2S}(t) \sim \text{Binom}\left(\Delta R_2(t), \frac{\rho_2}{\epsilon_{12}\text{FOI}_1(t) + \rho_2 + \mu}\right) \quad (\text{S63})$$

$$N_{R_2J_1}(t) \sim \text{Binom}\left(\Delta R_2(t), \frac{\epsilon_{12}\text{FOI}_1(t)}{\epsilon_{12}\text{FOI}_1(t) + \rho_2 + \mu}\right) \quad (\text{S64})$$

$$\Delta J_1(t) \sim \text{Binom}(J_1(t - \Delta t), 1 - \exp(-(\gamma_1 + \mu)\Delta t)) \quad (\text{S65})$$

$$N_{J_1R}(t) \sim \text{Binom}\left(\Delta J_1(t), \frac{\gamma_1}{\gamma_1 + \mu}\right) \quad (\text{S66})$$

$$\Delta J_2(t) \sim \text{Binom}(J_2(t - \Delta t), 1 - \exp(-(\gamma_2 + \mu)\Delta t)) \quad (\text{S67})$$

$$N_{J_2R}(t) \sim \text{Binom}\left(\Delta J_2(t), \frac{\gamma_2}{\gamma_2 + \mu}\right) \quad (\text{S68})$$

$$\Delta R(t) \sim \text{Binom}(R(t - \Delta t), 1 - \exp(-(\rho_1 + \rho_2 + \mu)\Delta t)) \quad (\text{S69})$$

$$N_{RR_1}(t) \sim \text{Binom}\left(\Delta R(t), \frac{\rho_1}{\rho_1 + \rho_2 + \mu}\right) \quad (\text{S70})$$

$$N_{RR_2}(t) \sim \text{Binom}\left(\Delta R(t), \frac{\rho_2}{\rho_1 + \rho_2 + \mu}\right) \quad (\text{S71})$$

$$S(t) = S(t - \Delta t) - \Delta S(t) + B(t) + N_{R_1S}(t) + N_{R_2S}(t) \quad (\text{S72})$$

$$I_1(t) = I_1(t - \Delta t) - \Delta I_1(t) + N_{SI_1}(t) \quad (\text{S73})$$

$$I_2(t) = I_2(t - \Delta t) - \Delta I_2(t) + N_{SI_2}(t) \quad (\text{S74})$$

$$R_1(t) = R_1(t - \Delta t) - \Delta R_1(t) + N_{I_1R_1}(t) + N_{RR_1}(t) \quad (\text{S75})$$

$$R_2(t) = R_2(t - \Delta t) - \Delta R_2(t) + N_{I_2R_2}(t) + N_{RR_2}(t) \quad (\text{S76})$$

$$J_1(t) = J_1(t - \Delta t) - \Delta J_1(t) + N_{R_2J_1}(t) \quad (\text{S77})$$

$$J_2(t) = J_2(t - \Delta t) - \Delta J_2(t) + N_{R_1J_2}(t) \quad (\text{S78})$$

$$R(t) = R(t - \Delta t) - \Delta R(t) + N_{J_1R}(t) + N_{J_2R}(t) \quad (\text{S79})$$

We simulated the model on a daily scale with previously estimated parameters for the RSV-HMPV interaction [34]: $b_1 = 1.7/\text{weeks}$, $b_2 = 1.95/\text{weeks}$, $\theta_1 = 0.4$, $\theta_2 = 0.3$, $\phi_1 = 0.005 \times 7/364$, $\phi_2 = 4.99 \times 7/364$, $\epsilon_{12} = 0.92$, $\epsilon_{21} = 0.45$, $\gamma_1 = 1/10/\text{days}$, $\gamma_2 = 1/10/\text{days}$, $\rho_1 = 1/364/\text{days}$, $\rho_2 = 1/364/\text{days}$, $\mu = 1/(70 \times 364)/\text{days}$, and $N = 1 \times 10^8$. The model was simulated from 1900 to 2030 assuming $S(0) = N - 200$, $I_1(0) = 100$, $I_2(0) = 100$, $R_1(0) = 0$, $R_2(0) = 0$, $J_1(0) = 0$, $J_2(0) = 0$, and $R(0) = 0$. The observed incidence for each strain is then simulated as follows:

$$C_1(t) = \text{Beta-Binom}(N_{SI_1}(t) + N_{R_2J_1}, \rho, k), \quad (\text{S80})$$

$$C_2(t) = \text{Beta-Binom}(N_{SI_2}(t) + N_{R_1J_2}, \rho, k), \quad (\text{S81})$$

where ρ represents the reporting probability and k represents the overdispersion parameter of beta-binomial distribution. We assumed $\rho = 0.002$ (i.e., 0.2% probability) and $k = 500$. We also considered the total incidence: $C_{\text{total}}(t) = C_1(t) + C_2(t)$.

For both models, we considered a more realistically shaped pandemic perturbation $\alpha(t)$ to challenge our ability to estimate the intervention effects. Thus, we

⁷⁷⁵ assumed a 40% transmission reduction for 3 months from March 2020, followed by a
⁷⁷⁶ 10% transmission reduction for 6 months, 20% transmission reduction for 3 months,
⁷⁷⁷ and a final return to normal levels:

$$\alpha(t) = \begin{cases} 1 & t < 2020.25 \\ 0.6 & 2020.25 \leq t < 2020.5 \\ 0.9 & 2020.5 \leq t < 2021 \\ 0.8 & 2021 \leq t < 2021.25 \\ 1 & 2021.25 \leq t \end{cases}. \quad (\text{S82})$$

⁷⁷⁸ For all simulations, we truncated the time series from the beginning of 2014 to the
⁷⁷⁹ end of 2023 and aggregated them into weekly cases.

⁷⁸⁰ To infer intrinsic resilience from time series, we fitted a simple discrete time,
⁷⁸¹ deterministic SIRS model in a Bayesian framework [4]:

$$\Delta t = 1 \text{ week} \quad (\text{S83})$$

$$\text{FOI}(t) = \beta(t)(I(t - \Delta t) + \omega)/N \quad (\text{S84})$$

$$\Delta S(t) = [1 - \exp(-(\text{FOI}(t) + \mu)\Delta t)] S(t - \Delta t) \quad (\text{S85})$$

$$N_{SI}(t) = \frac{\text{FOI}(t)\Delta S(t)}{\text{FOI}(t) + \mu} \quad (\text{S86})$$

$$\Delta I(t) = [1 - \exp(-(\gamma + \mu)\Delta t)] I(t - \Delta t) \quad (\text{S87})$$

$$N_{IR}(t) = \frac{\gamma \Delta I(t)}{\gamma + \mu} \quad (\text{S88})$$

$$\Delta R(t) = [1 - \exp(-(\nu + \mu)\Delta t)] R(t - \Delta t) \quad (\text{S89})$$

$$N_{RS}(t) = \frac{\nu \Delta R(t)}{\nu + \mu} \quad (\text{S90})$$

$$S(t) = S(t - \Delta t) + \mu S - \Delta S(t) + N_{RS}(t) \quad (\text{S91})$$

$$I(t) = I(t - \Delta t) - \Delta I(t) + N_{SI}(t) \quad (\text{S92})$$

$$R(t) = R(t - \Delta t) - \Delta R(t) + N_{IR}(t) \quad (\text{S93})$$

⁷⁸² where we include an extra term ω to account for importation. Although actual
⁷⁸³ simulations did not include any importation, we had found that including this term
⁷⁸⁴ generally helped with model convergence in previous analyses [4]. The transmission
⁷⁸⁵ rate was divided into a seasonal term $\beta_{\text{seas}}(t)$ (repeated every year) and intervention
⁷⁸⁶ term $\alpha(t)$, which were estimated jointly:

$$\beta(t) = \beta_{\text{seas}}(t)\alpha(t), \quad (\text{S94})$$

⁷⁸⁷ where $\alpha < 1$ corresponds to reduction in transmission due to intervention effects. To
⁷⁸⁸ constrain the smoothness of $\beta_{\text{seas}}(t)$, we imposed cyclic, random-walk priors:

$$\beta_{\text{seas}}(t) \sim \text{Normal}(\beta_{\text{seas}}(t - 1), \sigma) \quad t = 2 \dots 52 \quad (\text{S95})$$

$$\beta_{\text{seas}}(1) \sim \text{Normal}(\beta_{\text{seas}}(52), \sigma) \quad (\text{S96})$$

$$\sigma \sim \text{Half-Normal}(0, 1) \quad (\text{S97})$$

789 We fixed $\alpha(t) = 1$ for all $t < 2020$ and estimate α assuming a normal prior:

$$\alpha \sim \text{Normal}(1, 0.25). \quad (\text{S98})$$

790 We assumed weakly informative priors on ω and ν :

$$\omega \sim \text{Half-Normal}(0, 200) \quad (\text{S99})$$

$$\nu \sim \text{Normal}(104, 26) \quad (\text{S100})$$

791 We assumed that the true birth/death rates, population sizes, and recovery rates
792 are known. We note, however, that assuming $\gamma = 1/\text{week}$ actually corresponds to
793 a mean simulated infectious period of 1.6 weeks due to a time discretization, which
794 is much longer than the true value; this approximation allows us to test whether we
795 can still robustly estimate the intrinsic resilience given parameter mis-specification.
796 Initial conditions were estimated with following priors:

$$S(0) = Ns(0) \quad (\text{S101})$$

$$I(0) = Ni(0) \quad (\text{S102})$$

$$s(0) \sim \text{Uniform}(0, 1) \quad (\text{S103})$$

$$i(0) \sim \text{Half-Normal}(0, 0.001) \quad (\text{S104})$$

797 Finally, the observation model was specified as follows:

$$\text{Cases}(t) \sim \text{Negative-Binomial}(\rho N_{SI}(t), \phi) \quad (\text{S105})$$

$$\rho \sim \text{Half-Normal}(0, 0.02) \quad (\text{S106})$$

$$\phi \sim \text{Half-Normal}(0, 10) \quad (\text{S107})$$

798 where ρ represents the reporting probability and ϕ represents the negative binomial
799 overdispersion parameter.

800 The model was fitted to four separate time series: (1) incidence time series from
801 the SIRS model, (2) incidence time series for strain 1 from the two-strain model,
802 (3) incidence time series for strain 2 from the two-strain model, and (4) combined
803 incidence time series for strains 1 and 2 from the two-strain model. The model
804 was fitted using rstan [49, 50] with 4 chains, each consisting of 2000 iterations.
805 The resulting posterior distribution was used to calculate the intrinsic resilience of
806 the seasonally unforced SIRS model with the same parameters; eigenvalues of the
807 discrete-time SIR model were computed by numerically finding the equilibrium and
808 calculating the Jacobian matrix.

809 **Validations for window-selection criteria**

810 We used stochastic SIRS simulations to identify optimal parameters for the window-
 811 selection criteria that we used for the linear regression for estimating empirical re-
 812 silience. For each simulation, we began by generating a random perturbation $\alpha(t)$
 813 from a random set of parameters. First, we drew the duration of perturbation τ_{npi}
 814 from a uniform distribution between 1 and 2 years. Then, we drew independent
 815 normal variables z_i of length $[364\tau_{\text{npi}}]$ with a standard deviation of 0.02 and took a
 816 reverse cumulative sum to obtain a realistic shape for the perturbation:

$$x_n = 1 + \sum_{i=n}^{[364\tau_{\text{npi}}]} z_i, \quad n = 1, \dots, [364\tau_{\text{npi}}]. \quad (\text{S108})$$

817 In contrast to simple perturbations that assume a constant reduction in transmis-
 818 sion, this approach allows us to model transmission reduction that varies over time
 819 smoothly. We repeated this random generation process until less than 10% of x_n
 820 exceeds 1—this was done to ensure the perturbation term $\alpha(t)$ stays below 1 (and
 821 therefore reduce transmission) for the most part. Then, we set any values that are
 822 above 1 or below 0 to 1 and 0, respectively. Then, we randomly drew the minimum
 823 transmission during perturbation α_{\min} from a uniform distribution between 0.5 and
 824 0.7 and scale x_n to have a minimum of α_{\min} :

$$x_{\text{scale},n} = \alpha_{\min} + (1 - \alpha_{\min}) \times \frac{x_n - \min x_n}{1 - \min x_n}. \quad (\text{S109})$$

825 This allowed us to simulate a realistically shaped perturbation:

$$\alpha(t) = \begin{cases} 1 & t < 2020 \\ x_{\text{scale},364(t-2020)} & 2020 \leq t < 2020 + \tau_{\text{npi}} \\ 1 & \tau_{\text{npi}} \leq t \end{cases}. \quad (\text{S110})$$

826 Given this perturbation function, we draw \mathcal{R}_0 from a uniform distribution between
 827 1.5 and 4 and the mean duration of immunity $1/\delta$ from a uniform distribution be-
 828 tween 1 and 4. Then, we simulate the stochastic SIRS model from $S(0) = 10^8/\mathcal{R}_0$
 829 and $I(0) = 100$ from 1990 to 2025 and truncate the time series to 2014–2025; if the
 830 epidemic becomes extinct before the end of simulation, we discard that simulation
 831 and start over from the perturbation generation step.

832 For each epidemic simulation, we computed the empirical resilience by varying
 833 the threshold R for the nearest neighbor approach from 4 to 14 with increments of
 834 2, the number of divisions K for the window selection between 8 and 25, and the
 835 truncation threshold a for the window selection between 1 to 3; this was done for all
 836 possible combinations of R , K , and a . We also compared this with the naive approach
 837 that uses the entire distance-from-attractor time series, starting from the maximum
 838 distance to the end of the time series. We repeated this procedure 500 times and
 839 quantified the correlation between empirical and intrinsic resilience estimates across
 840 two approaches.

Supplementary Figures

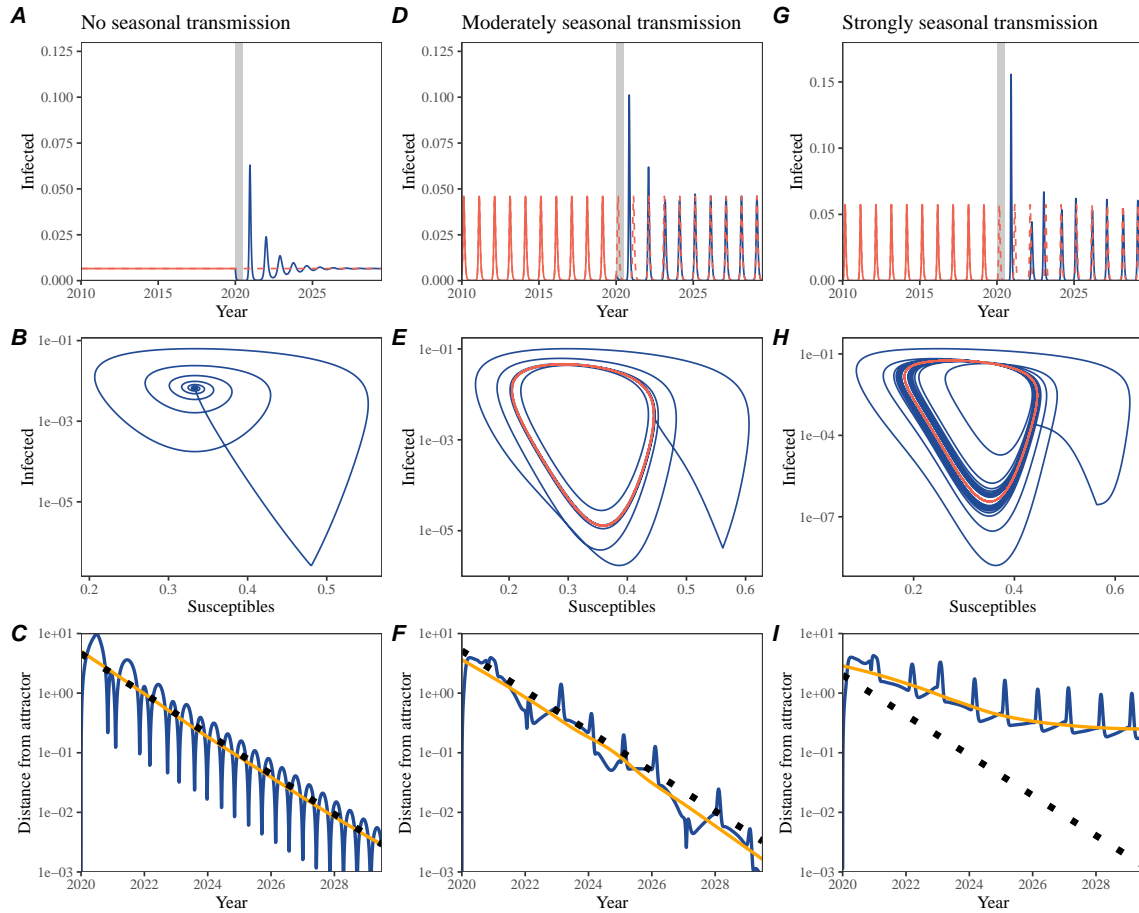


Figure S1: Impact of seasonal transmission on pathogen resilience. (A, D, G) Simulated epidemic trajectories using the SIRS model without seasonal forcing (A), with seasonal forcing of amplitude of 0.2 (D), and with seasonal forcing of amplitude of 0.4 (G). Red and blue solid lines represent epidemic dynamics before and after interventions are introduced, respectively. Red dashed lines represent counterfactual epidemic dynamics in the absence of interventions. Gray regions indicate the duration of interventions. (B, E, H) Phase plane representation of the time series in panels A, D, and G alongside the corresponding susceptible host dynamics. Red and blue solid lines represent epidemic trajectories on an SI phase plane before and after interventions are introduced, respectively. (C, F, I) Changes in logged distance from the attractor over time. Blue lines represent the logged distance from the attractor. Orange lines represent the locally estimated scatterplot smoothing (LOESS) fits to the logged distance from the attractor. Dotted lines show the intrinsic resilience of the seasonally unforced system.

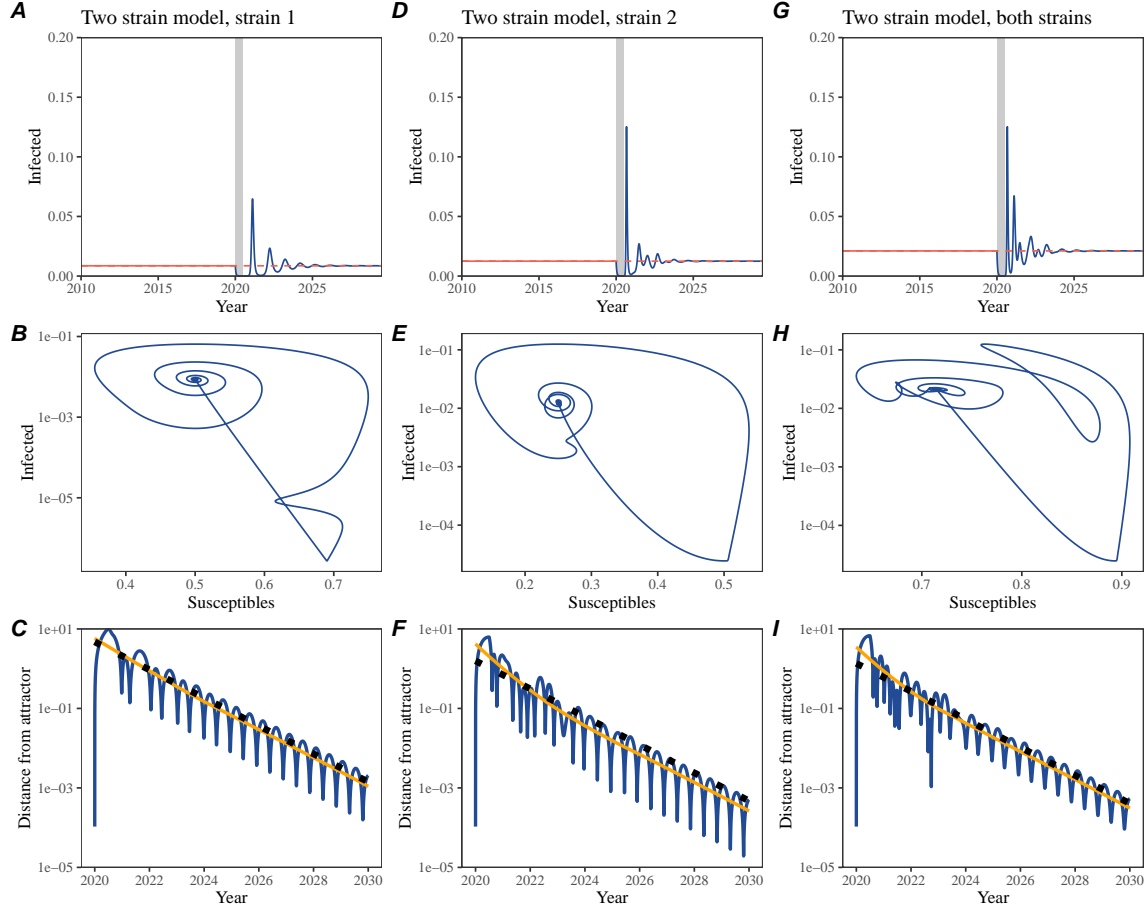


Figure S2: A simple method to measure pathogen resilience following pandemic perturbations for a two-strain competition system without seasonal forcing. (A, D, G) Simulated epidemic trajectories using a two-strain system without seasonal forcing. In this model, two strains compete through cross immunity. Red and blue solid lines represent epidemic dynamics before and after interventions are introduced, respectively. Red dashed lines represent counterfactual epidemic dynamics in the absence of interventions. Gray regions indicate the duration of interventions. (B, E, H) Phase plane representation of the time series in panels A, D, and G alongside the corresponding susceptible host dynamics. Blue solid lines represent epidemic trajectories on an SI phase plane before and after interventions. (C, F, I) Changes in logged distance from the attractor over time. Blue lines represent the logged distance from the attractor. Orange lines represent the locally estimated scatterplot smoothing (LOESS) fits to the logged distance from the attractor. Dotted lines show the intrinsic resilience of the seasonally unforced system.

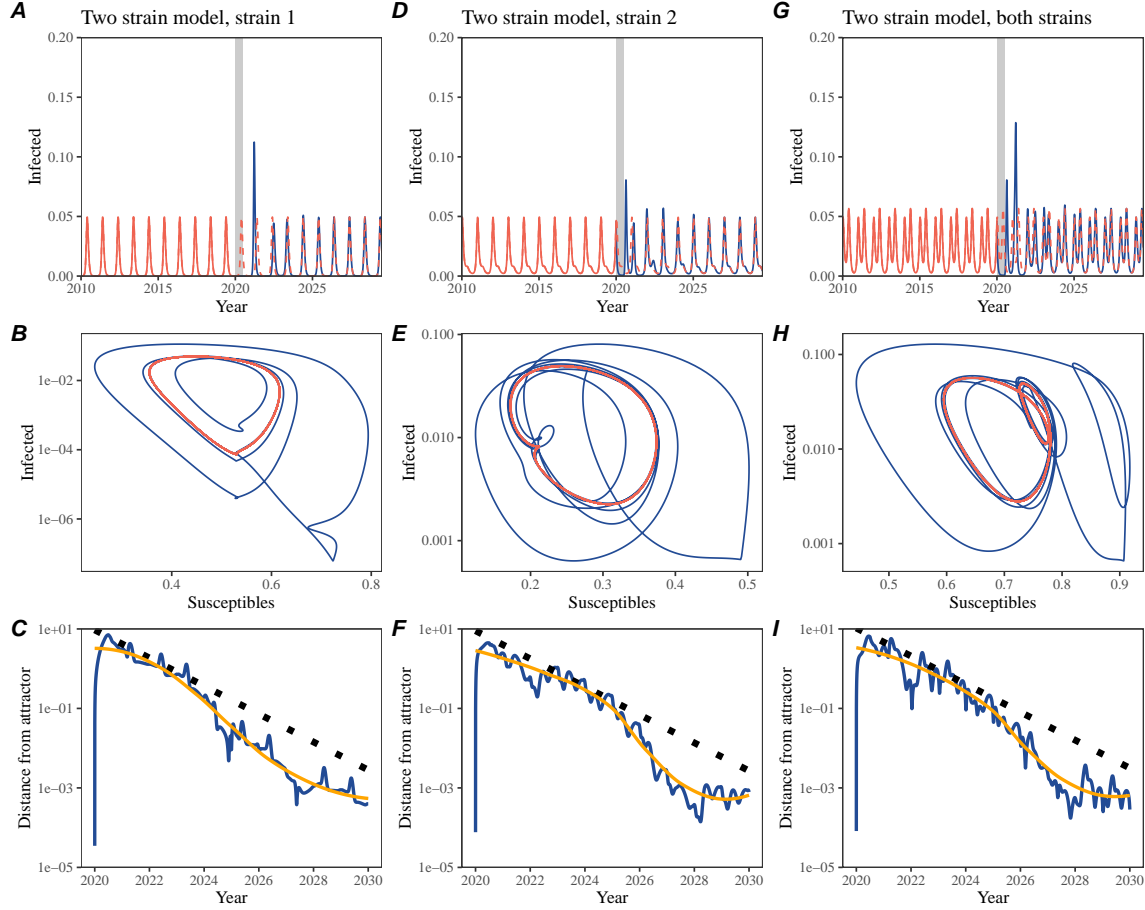


Figure S3: A simple method to measure pathogen resilience following pandemic perturbations for a two-strain competition system with seasonal forcing. (A, D, G) Simulated epidemic trajectories using a two-strain system with seasonal forcing (amplitude of 0.2). In this model, two strains compete through cross immunity. Red and blue solid lines represent epidemic dynamics before and after interventions are introduced, respectively. Red dashed lines represent counterfactual epidemic dynamics in the absence of interventions. Gray regions indicate the duration of interventions. (B, E, H) Phase plane representation of the time series in panels A, D, and G alongside the corresponding susceptible host dynamics. Red and blue solid lines represent epidemic trajectories on an SI phase plane before and after interventions are introduced, respectively. (C, F, I) Changes in logged distance from the attractor over time. Blue lines represent the logged distance from the attractor. Orange lines represent the locally estimated scatterplot smoothing (LOESS) fits to the logged distance from the attractor. Dotted lines show the intrinsic resilience of the seasonally unforced system.

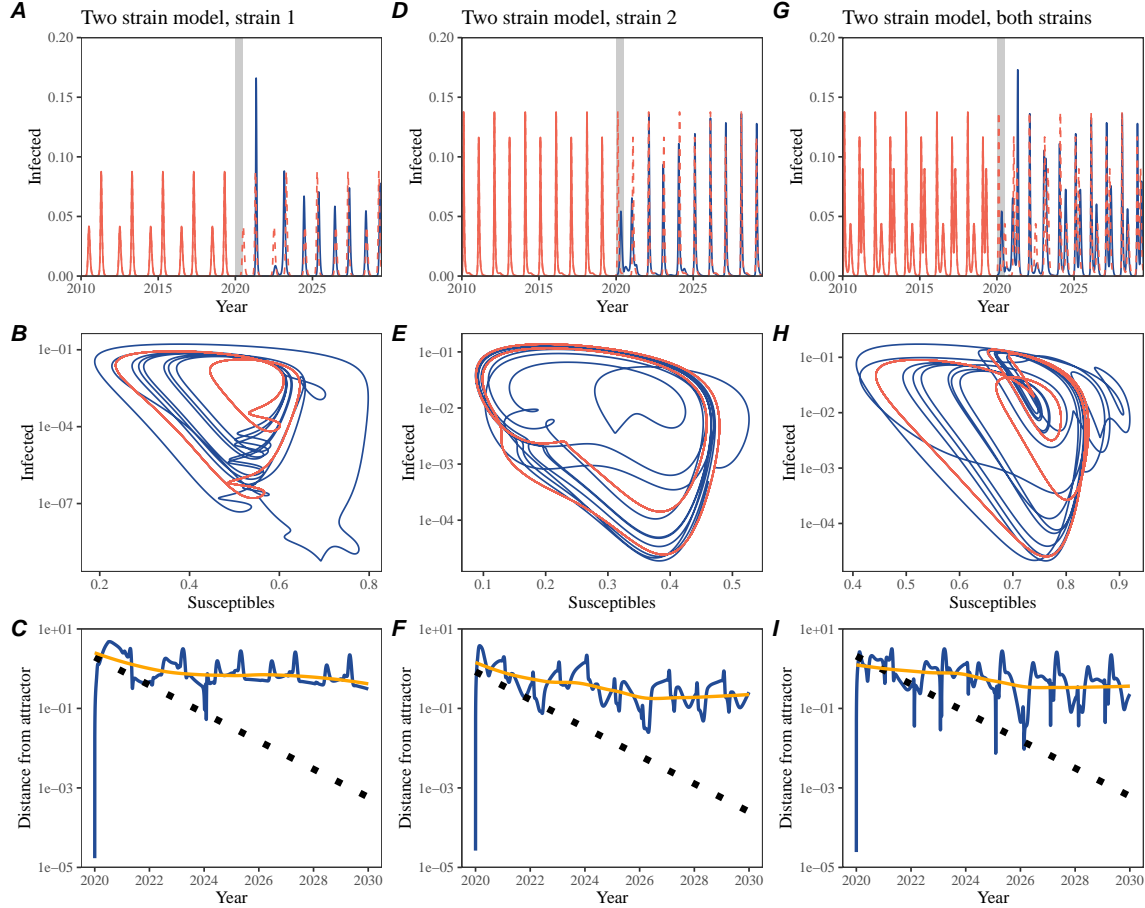


Figure S4: A simple method to measure pathogen resilience following pandemic perturbations for a multi-strain competition system with strong seasonal forcing. (A, D, G) Simulated epidemic trajectories using a two-strain system with seasonal forcing (amplitude of 0.2). In this model, two strains compete through cross immunity. Red and blue solid lines represent epidemic dynamics before and after interventions are introduced, respectively. Red dashed lines represent counterfactual epidemic dynamics in the absence of interventions. Gray regions indicate the duration of interventions. (B, E, H) Phase plane representation of the time series in panels A, D, and G alongside the corresponding susceptible host dynamics. Red and blue solid lines represent epidemic trajectories on an SI phase plane before and after interventions are introduced, respectively. (C, F, I) Changes in logged distance from the attractor over time. Blue lines represent the logged distance from the attractor. Orange lines represent the locally estimated scatterplot smoothing (LOESS) fits to the logged distance from the attractor. Dotted lines show the intrinsic resilience of the seasonally unforced system.

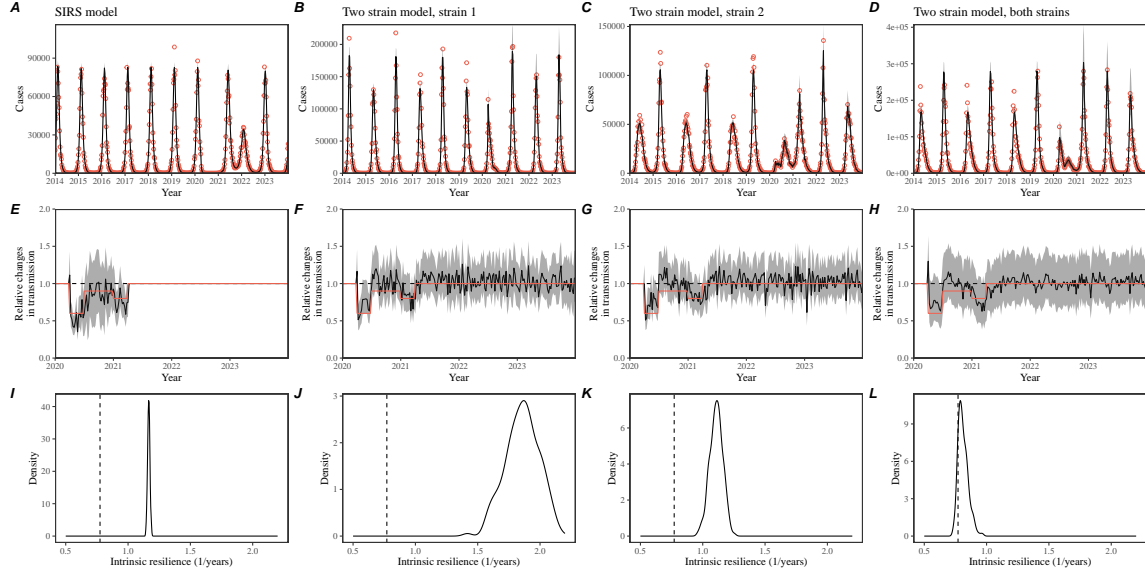


Figure S5: Mechanistic model fits to simulated data and inferred intrinsic resilience. We simulated discrete time, stochastic epidemic trajectories using a seasonally forced SIRS model (A,E,I) and a seasonally forced two-strain model (B–D, F–H, and J–L) and tested whether we can estimate the intrinsic resilience of the seasonally unforced versions of the model by fitting a mechanistic model (Supplementary Text). We fitted the same discrete time, one strain, deterministic SIRS model in each scenario. (A–D) Simulated case time series from corresponding models shown in the title (red) and SIRS model fits (black). (E–H) Assumed changes in transmission due to pandemic perturbations (red) and estimated time-varying relative transmission rates for the perturbation impact from the SIRS model fits (black). Solid lines and shaded regions represent fitted posterior median and 95% credible intervals. (I–L) Comparisons between the true and estimated intrinsic resilience of the seasonally unforced system. Vertical lines represent the true intrinsic resilience of the seasonally unforced system. Density plots represent the posterior distribution of the inferred intrinsic resilience of the seasonally unforced SIRS model using fitted parameters.

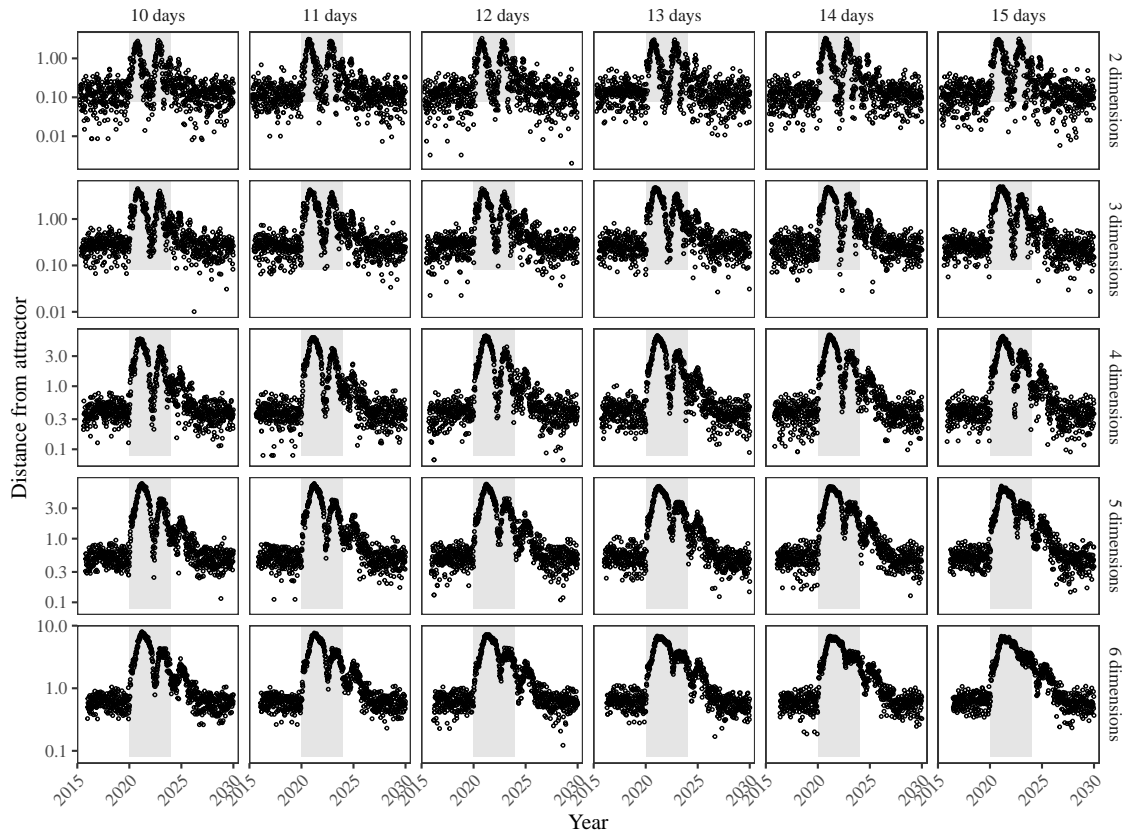


Figure S6: Sensitivity of the distance from the attractor to choice of embedding lags and dimensions. Sensitivity analysis for the distance-from-attractor time series shown in Figure 3E in the main text by varying the embedding lag between 10–15 days and embedding dimensions between 2–6 dimensions. The gray region represents the assumed period of pandemic perturbation.

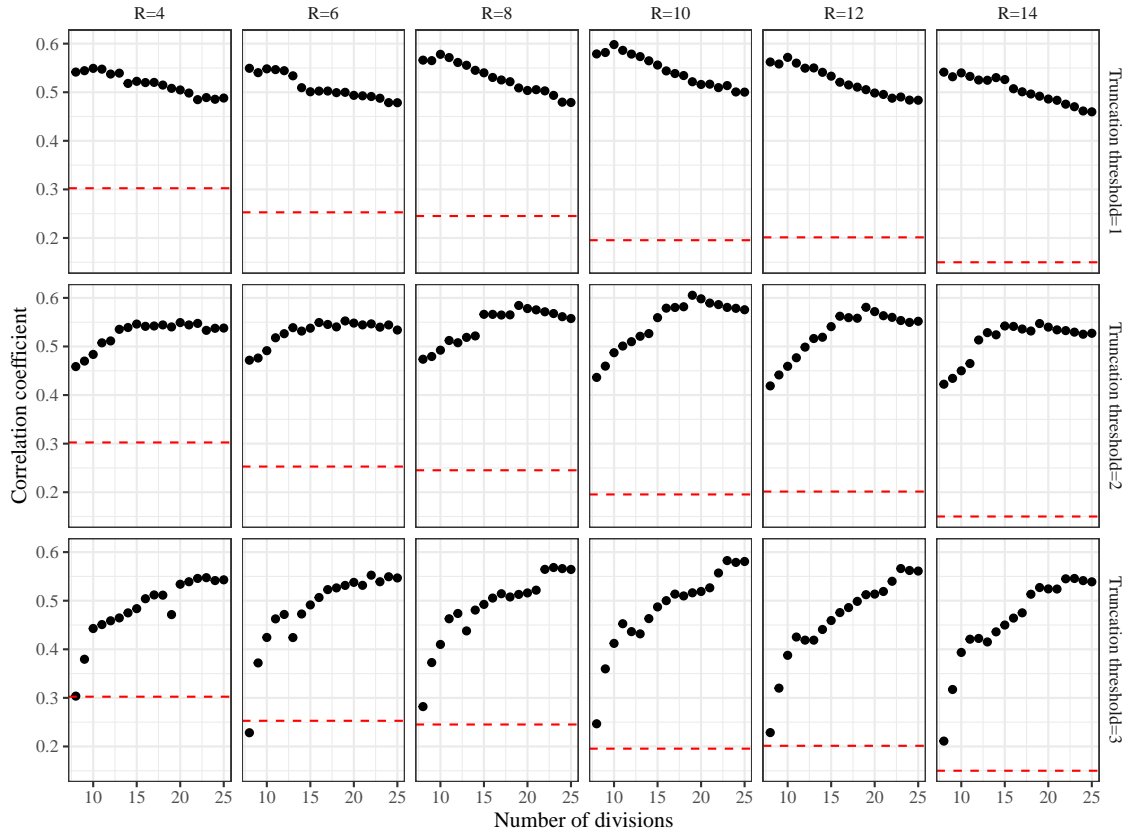


Figure S7: Impact of fitting window selection on the estimation of empirical resilience. We simulated 500 epidemics of a stochastic SIRS model with randomly drawn parameters and randomly generated pandemic perturbations (Supplementary Text). For each simulation, we varied the false nearest neighbor threshold R for reconstructing the empirical attractor as well as the parameters for regression window selection (i.e., the truncation threshold a and the number of divisions K). Each point represents the resulting correlation coefficient between empirical and intrinsic resilience estimates for a given scenario. Dashed lines represent the correlation coefficient between empirical and intrinsic resilience estimates for the naive approach that fits a linear regression on a log scale, starting from the maximum distance until the end of the time series.

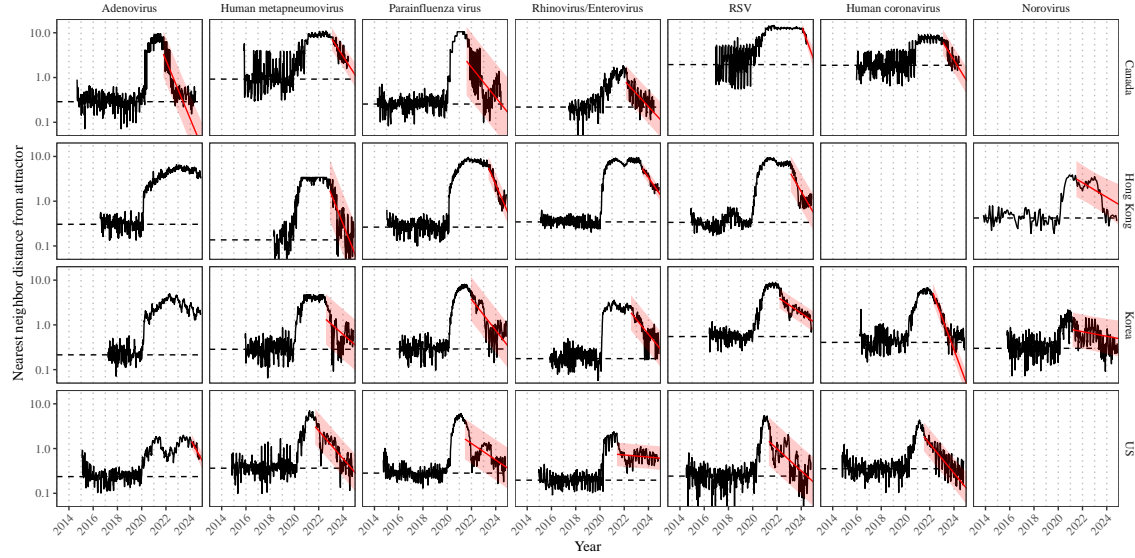


Figure S8: Estimated time series of distance from the attractor for each pathogen and corresponding linear regression fits using automated window selection criteria across Canada, Hong Kong, Korea, and the US. Black lines represent the estimated distance from the attractor. Red lines and shaded regions represent the linear regression fits and corresponding 95% confidence intervals. Dashed lines represent the average of the pre-pandemic nearest neighbor distances.

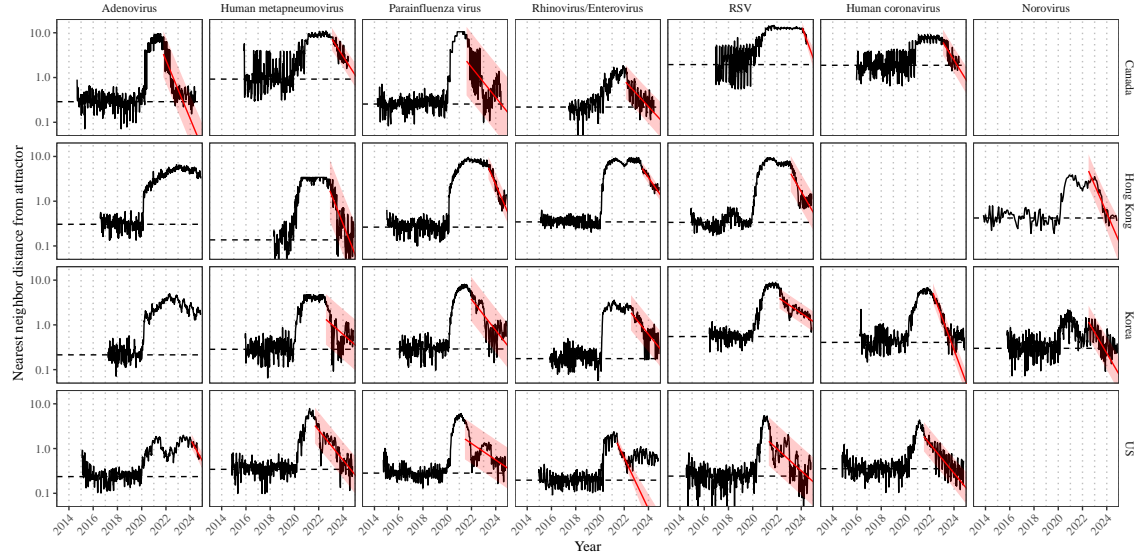


Figure S9: Estimated time series of distance from the attractor for each pathogen and corresponding linear regression fits across Canada, Hong Kong, Korea, and the US, including ad-hoc regression window selection. We used ad-hoc regression windows for norovirus in Hong Kong and Korea and rhinovirus/enterovirus in the US. Black lines represent the estimated distance from the attractor. Red lines and shaded regions represent the linear regression fits and corresponding 95% confidence intervals. Dashed lines represent the average of the pre-pandemic nearest neighbor distances.

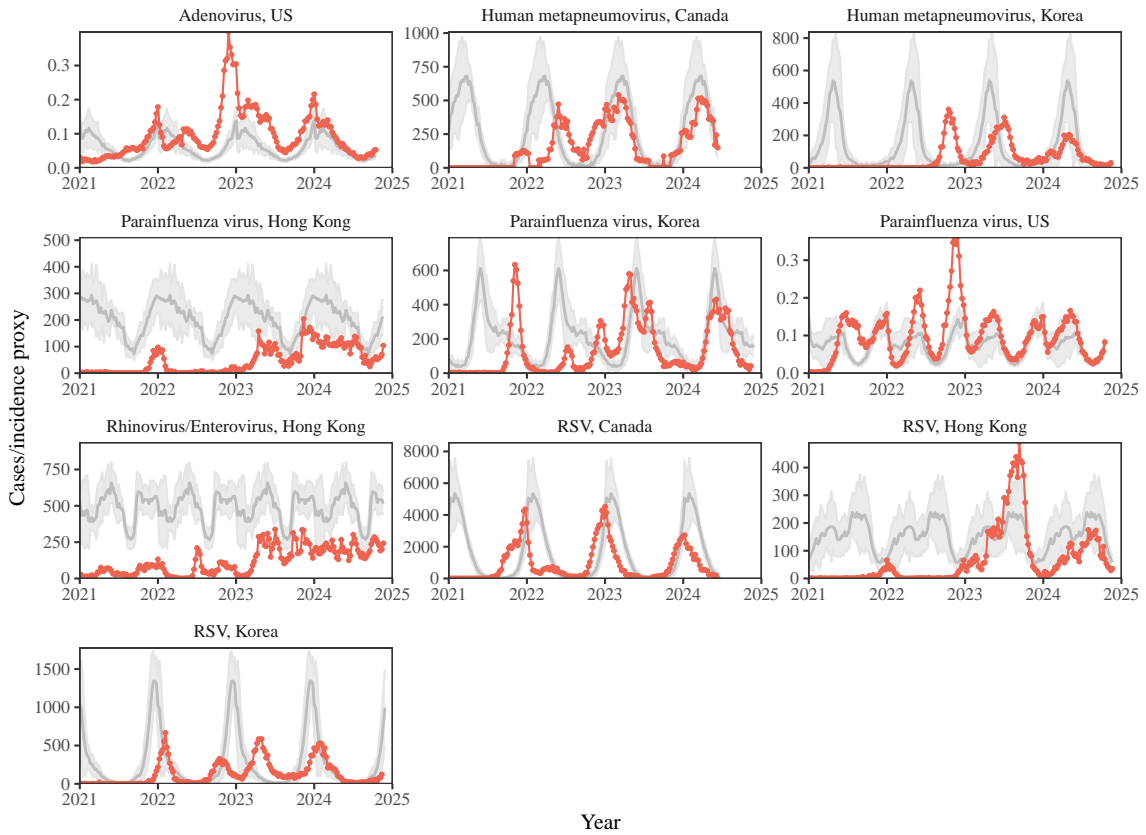


Figure S10: Observed dynamics for pathogen that are predicted to return after the end of 2024. Red points and lines represent data before 2020. Gray lines and shaded regions represent the mean seasonal patterns and corresponding 95% confidence intervals around the mean, previously shown in Figure 1.

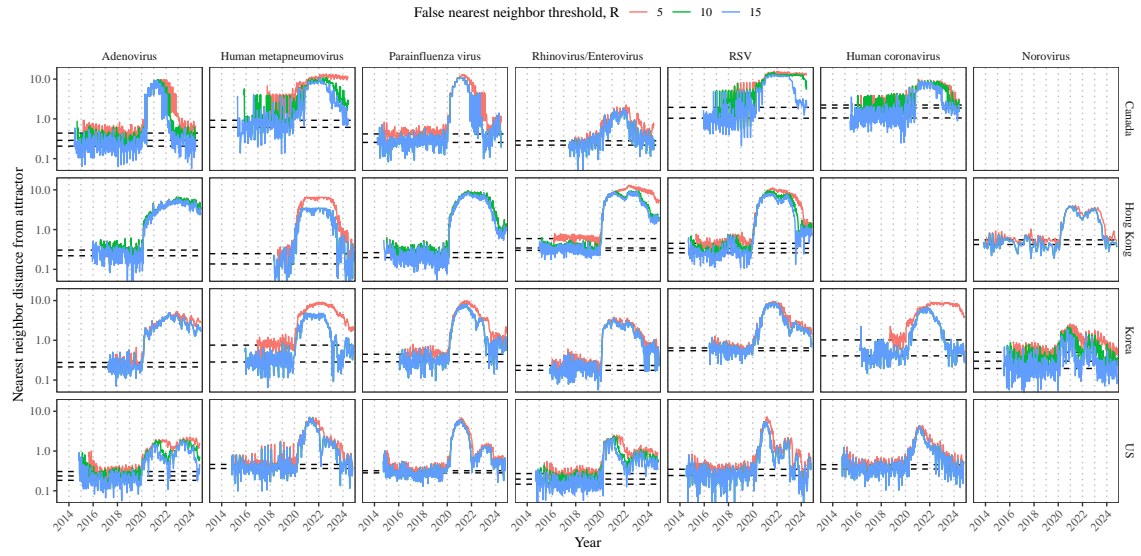


Figure S11: Estimated time series of distance from the attractor for each pathogen across different choices about false nearest neighbor threshold values. Using higher threshold values for the false nearest neighbor approach gives lower embedding dimensions. Colored lines represent the estimated distance from the attractor for different threshold values.

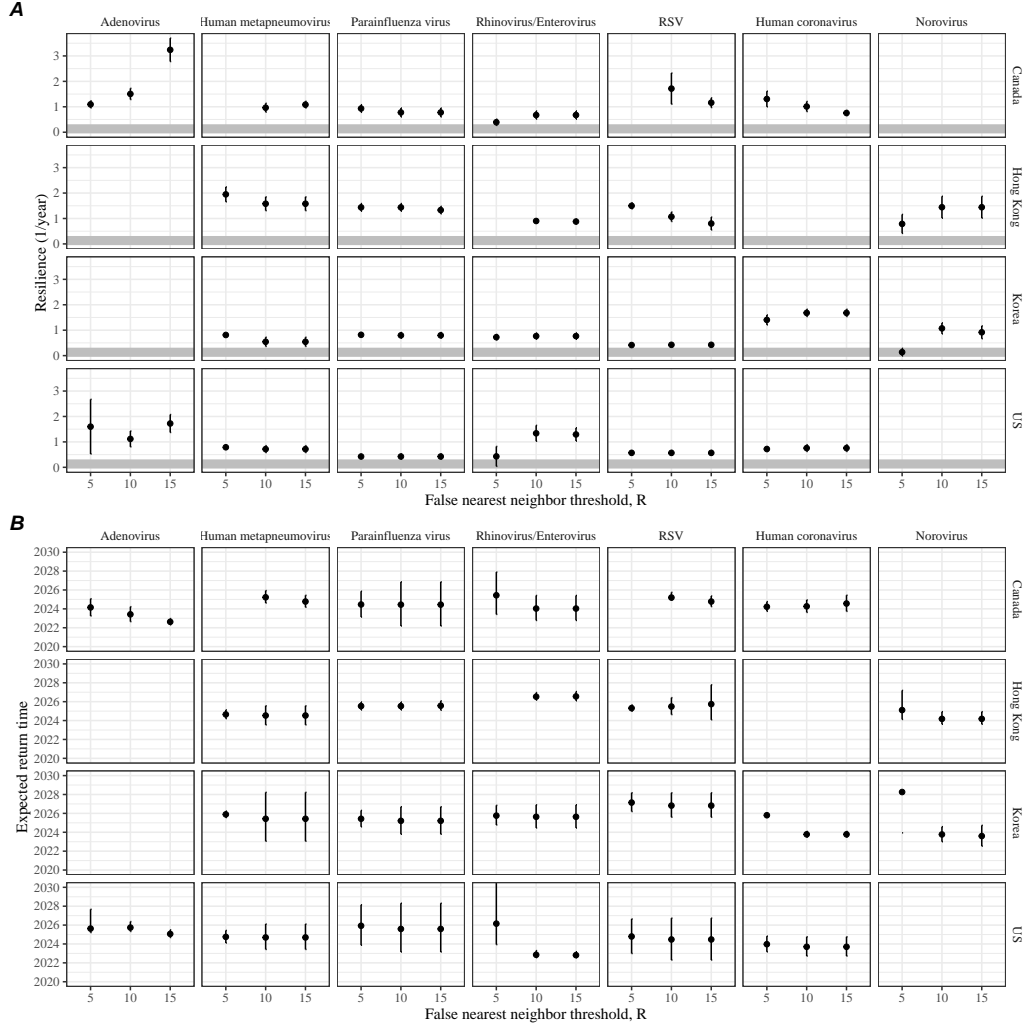


Figure S12: Summary of resilience estimates and predictions for return time across different choices about false nearest neighbor threshold values. The automated window selection method was used for all scenarios to estimate pathogen resilience, except for norovirus in Hong Kong and Korea and rhinovirus/enterovirus in the US. We used the same ad-hoc regression windows for norovirus in Hong Kong and Korea and rhinovirus/enterovirus in the US as we did in the main analysis. (A) Estimated pathogen resilience. The gray horizontal line represents the intrinsic resilience of pre-vaccination measles dynamics. (B) Predicted timing of when each pathogen will return to their pre-pandemic cycles. The dashed line in panel B indicates the end of 2024. Error bars represent 95% confidence intervals.

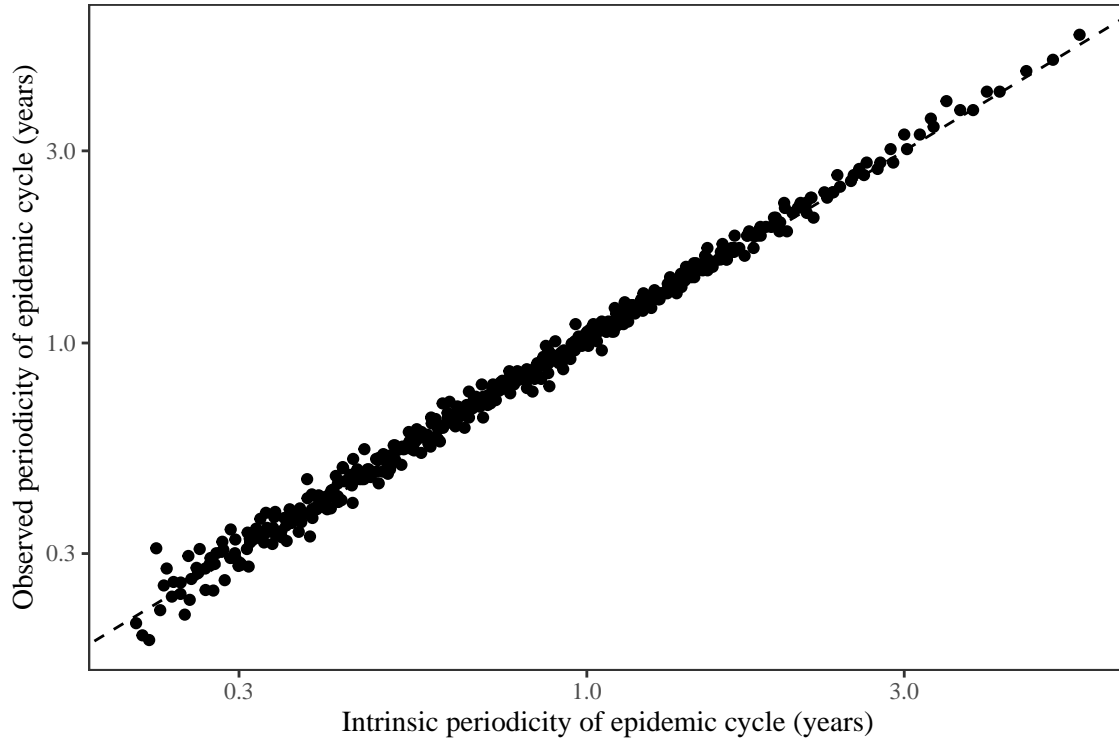


Figure S13: **Comparison between the observed and intrinsic periodicity of the epidemic cycle of the seasonally unforced SIRS model.** The observed periodicity of the epidemic corresponds to the periodicity at which maximum spectral density occurs. The intrinsic periodicity of the epidemic corresponds to $2\pi/\text{Im}(\lambda)$, where $\text{Im}(\lambda)$ is the imaginary part of the eigenvalue.

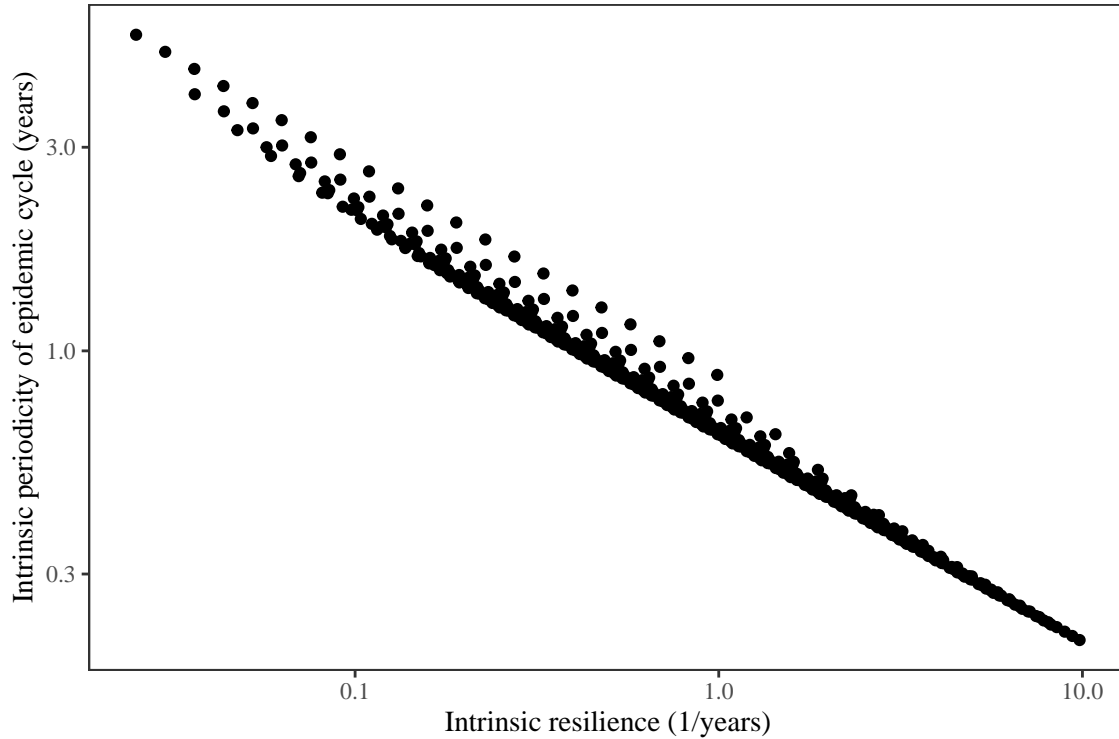


Figure S14: **Comparison between the intrinsic resilience and periodicity of the epidemic cycle of the seasonally unforced SIRS model.** The intrinsic resilience of the epidemic corresponds to the negative of the real value of the eigenvalue $-\text{Re}(\lambda)$. The intrinsic periodicity of the epidemic corresponds to $2\pi/\text{Im}(\lambda)$, where $\text{Im}(\lambda)$ is the imaginary part of the eigenvalue.

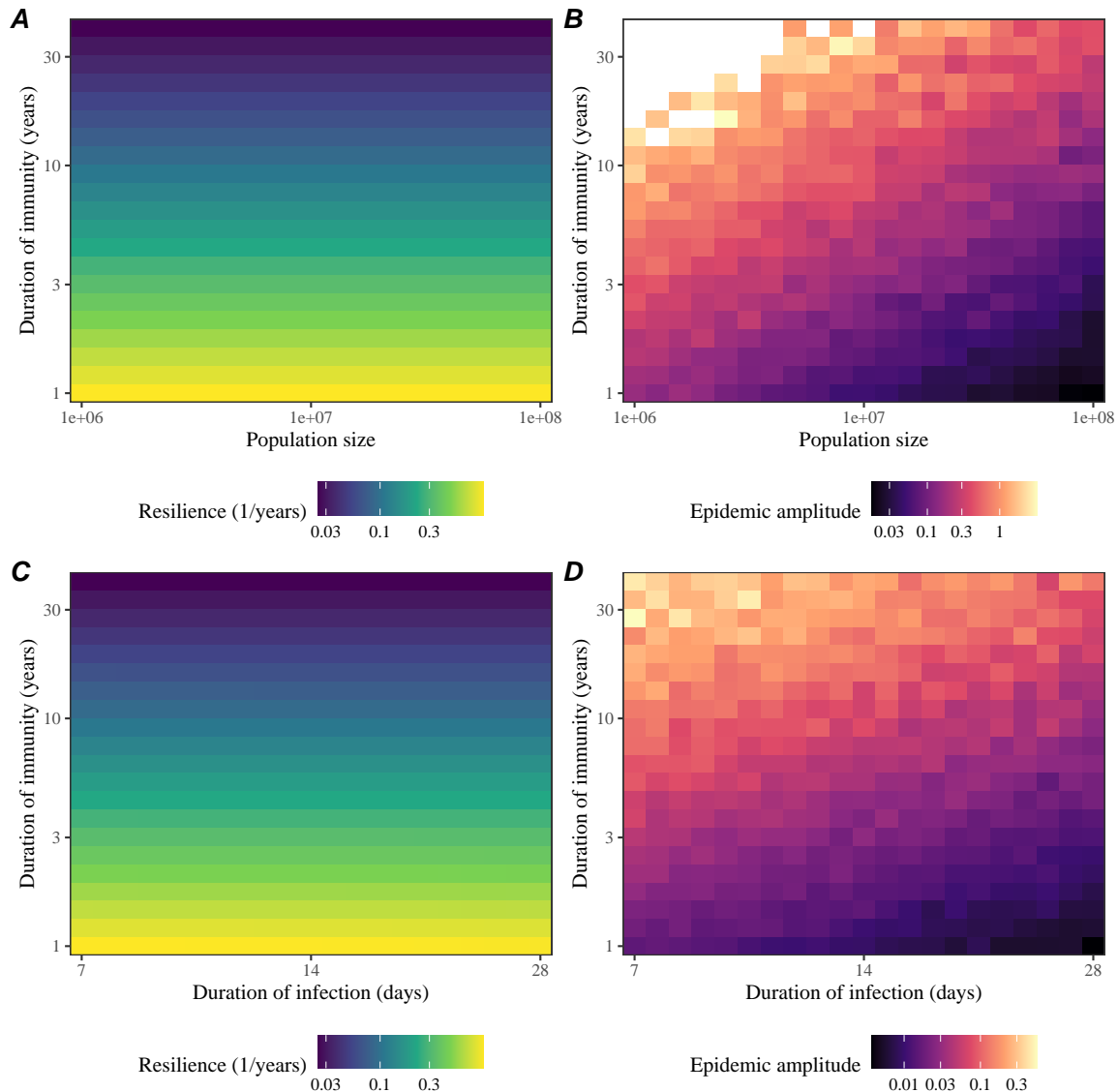


Figure S15: **Impact of population size and the average duration of infection of a host-pathogen system on its sensitivity to stochastic perturbations.** (A) Intrinsic resilience of a system as a function of population size and the average duration of immunity. (B) Epidemic amplitude as a function of population size and the average duration of immunity. (C) Intrinsic resilience of a system as a function of the average duration of infection and immunity. (D) Epidemic amplitude as a function of the average duration of infection and immunity. The epidemic amplitude corresponds to $(\max I - \min I)/(2\bar{I})$, where \bar{I} represents the mean prevalence.

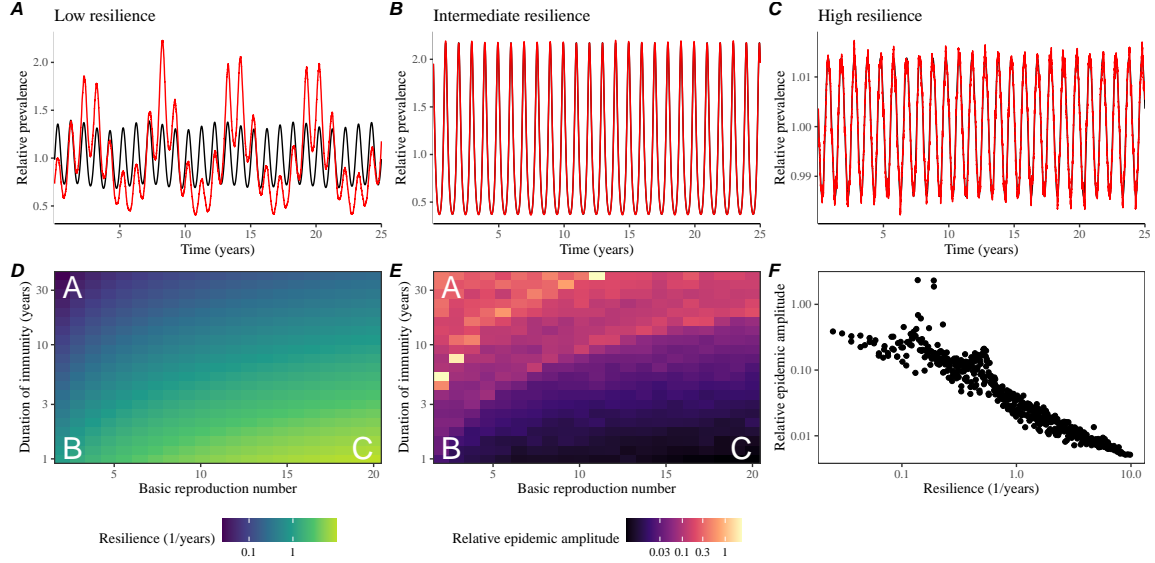


Figure S16: Linking resilience of a host-pathogen system to its sensitivity to stochastic perturbations for the seasonally forced SIRS model. (A–C) Epidemic trajectories of a stochastic SIRS model with demographic stochasticity across three different resilience values: low, intermediate, and high. The relative prevalence was calculated by dividing infection prevalence by its mean value. Black lines represent deterministic epidemic trajectories. Red lines represent stochastic epidemic trajectories. (D) The intrinsic resilience of the seasonally unforced system as a function of the basic reproduction number \mathcal{R}_0 and the duration of immunity. (E) The relative epidemic amplitude, a measure of sensitivity to stochastic perturbations, as a function of the basic reproduction number \mathcal{R}_0 and the duration of immunity. To calculate the relative epidemic amplitude, we first take the relative difference in infection prevalence between stochastic and deterministic trajectories: $\epsilon = (I_{\text{stoch}} - I_{\text{det}})/I_{\text{det}}$. Then, we calculate the difference between maximum and minimum of the relative difference and divide by half: $(\max \epsilon - \min \epsilon)/2$. Labels A–C in panels D and E correspond to scenarios shown in panels A–C. (F) The relationship between pathogen resilience and relative epidemic amplitude.

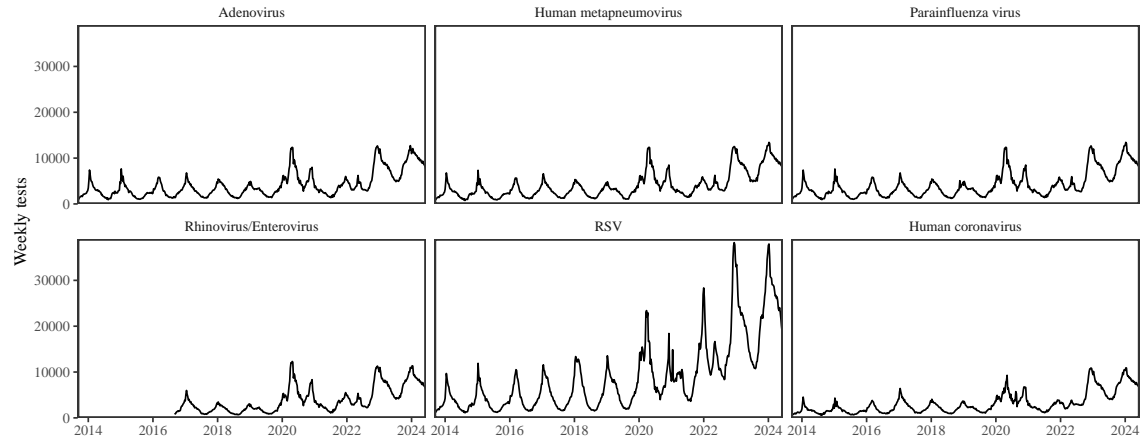


Figure S17: Testing patterns for respiratory pathogens in Canada.

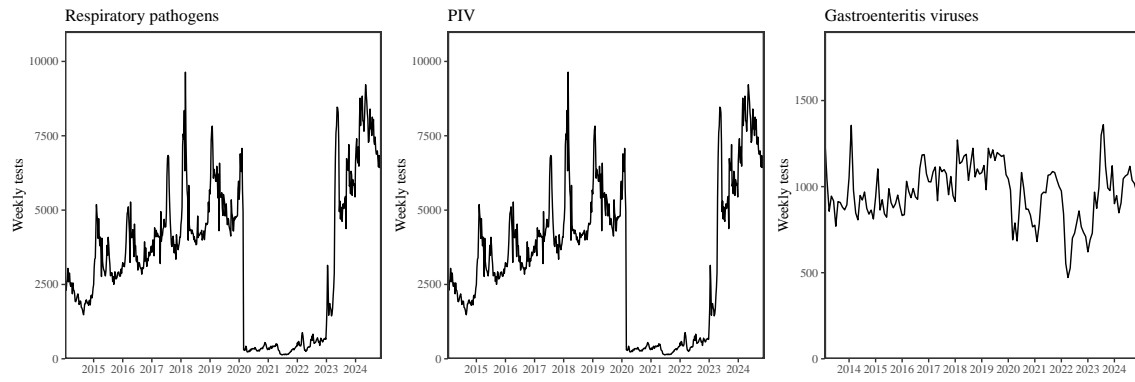


Figure S18: Testing patterns for respiratory pathogens, PIV, and gastroenteritis viruses in Hong Kong.

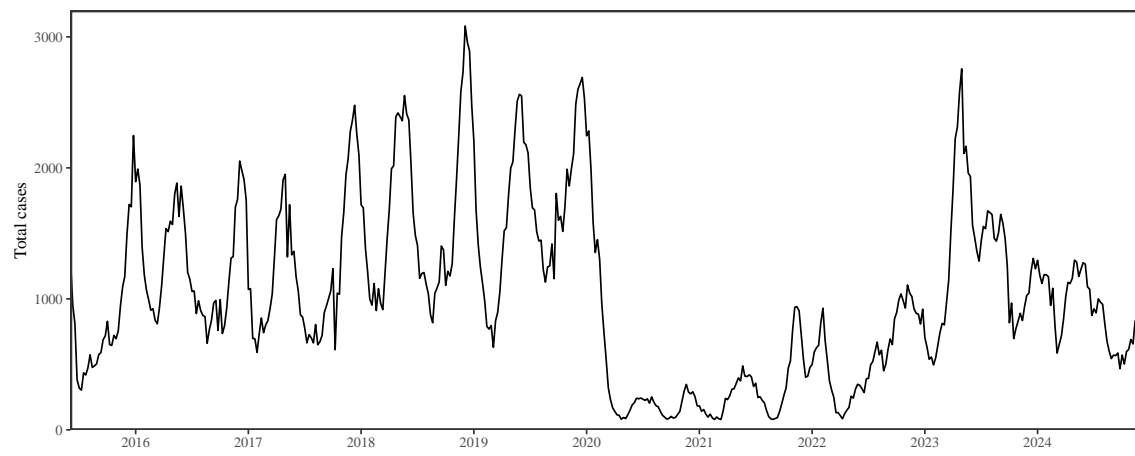


Figure S19: Total number of reported respiratory infection cases in Korea.

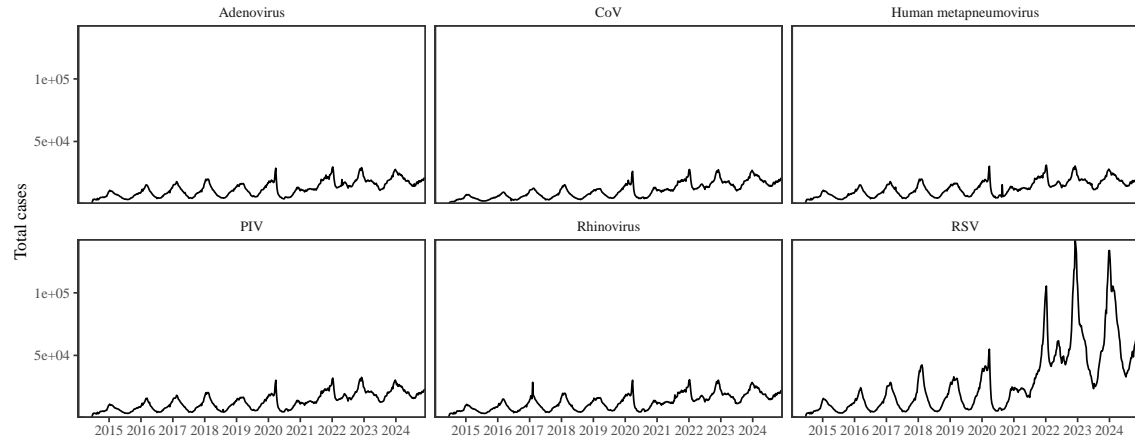


Figure S20: Testing patterns for respiratory pathogens in the US reported through the NREVSS.

842 References

- 843 [1] Rachel E Baker, Sang Woo Park, Wenchang Yang, Gabriel A Vecchi, C Jessica E
844 Metcalf, and Bryan T Grenfell. The impact of COVID-19 nonpharmaceutical
845 interventions on the future dynamics of endemic infections. *Proceedings of the*
846 *National Academy of Sciences*, 117(48):30547–30553, 2020.
- 847 [2] Gabriela B Gomez, Cedric Mahé, and Sandra S Chaves. Uncertain effects of the
848 pandemic on respiratory viruses. *Science*, 372(6546):1043–1044, 2021.
- 849 [3] Mihaly Koltai, Fabienne Krauer, David Hodgson, Edwin van Leeuwen, Marina
850 Treskova-Schwarzbach, Mark Jit, and Stefan Flasche. Determinants of RSV
851 epidemiology following suppression through pandemic contact restrictions. *Epi-*
852 *demics*, 40:100614, 2022.
- 853 [4] Sang Woo Park, Brooklyn Noble, Emily Howerton, Bjarke F Nielsen, Sarah
854 Lentz, Lilliam Ambroggio, Samuel Dominguez, Kevin Messacar, and Bryan T
855 Grenfell. Predicting the impact of non-pharmaceutical interventions against
856 COVID-19 on *Mycoplasma pneumoniae* in the United States. *Epidemics*,
857 49:100808, 2024.
- 858 [5] Amanda C Perofsky, Chelsea L Hansen, Roy Burstein, Shanda Boyle, Robin
859 Prentice, Cooper Marshall, David Reinhart, Ben Capodanno, Melissa Truong,
860 Kristen Schwabe-Fry, et al. Impacts of human mobility on the citywide trans-
861 mission dynamics of 18 respiratory viruses in pre-and post-COVID-19 pandemic
862 years. *Nature communications*, 15(1):4164, 2024.
- 863 [6] Eric J Chow, Timothy M Uyeki, and Helen Y Chu. The effects of the COVID-19
864 pandemic on community respiratory virus activity. *Nature Reviews Microbiol-*
865 *ogy*, 21(3):195–210, 2023.
- 866 [7] Stephen M Kissler, Christine Tedijanto, Edward Goldstein, Yonatan H Grad,
867 and Marc Lipsitch. Projecting the transmission dynamics of SARS-CoV-2
868 through the postpandemic period. *Science*, 368(6493):860–868, 2020.
- 869 [8] Rachel E Baker, Chadi M Saad-Roy, Sang Woo Park, Jeremy Farrar, C Jessica E
870 Metcalf, and Bryan T Grenfell. Long-term benefits of nonpharmaceutical inter-
871 ventions for endemic infections are shaped by respiratory pathogen dynamics.
872 *Proceedings of the National Academy of Sciences*, 119(49):e2208895119, 2022.
- 873 [9] Maaike C Swets, Clark D Russell, Ewen M Harrison, Annemarie B Docherty,
874 Nazir Lone, Michelle Girvan, Hayley E Hardwick, Leonardus G Visser, Pe-
875 ter JM Openshaw, Geert H Groeneveld, et al. SARS-CoV-2 co-infection with
876 influenza viruses, respiratory syncytial virus, or adenoviruses. *The Lancet*,
877 399(10334):1463–1464, 2022.

- 878 [10] Chun-Yang Lin, Joshua Wolf, David C Brice, Yilun Sun, Macauley Locke,
879 Sean Cherry, Ashley H Castellaw, Marie Wehenkel, Jeremy Chase Crawford,
880 Veronika I Zarnitsyna, et al. Pre-existing humoral immunity to human common
881 cold coronaviruses negatively impacts the protective SARS-CoV-2 antibody re-
882 sponse. *Cell host & microbe*, 30(1):83–96, 2022.
- 883 [11] Sam M Murray, Azim M Ansari, John Frater, Paul Klenerman, Susanna
884 Dunachie, Eleanor Barnes, and Ane Ogbe. The impact of pre-existing cross-
885 reactive immunity on SARS-CoV-2 infection and vaccine responses. *Nature*
886 *Reviews Immunology*, 23(5):304–316, 2023.
- 887 [12] John-Sebastian Eden, Chisha Sikazwe, Ruopeng Xie, Yi-Mo Deng, Sheena G
888 Sullivan, Alice Michie, Avram Levy, Elena Cutmore, Christopher C Blyth,
889 Philip N Britton, et al. Off-season RSV epidemics in Australia after easing
890 of COVID-19 restrictions. *Nature communications*, 13(1):2884, 2022.
- 891 [13] Stuart L Pimm. The structure of food webs. *Theoretical population biology*,
892 16(2):144–158, 1979.
- 893 [14] Michael G Neubert and Hal Caswell. Alternatives to resilience for measuring
894 the responses of ecological systems to perturbations. *Ecology*, 78(3):653–665,
895 1997.
- 896 [15] Lance H Gunderson. Ecological resilience—in theory and application. *Annual*
897 *review of ecology and systematics*, 31(1):425–439, 2000.
- 898 [16] Vasilis Dakos and Sonia Kéfi. Ecological resilience: what to measure and how.
899 *Environmental Research Letters*, 17(4):043003, 2022.
- 900 [17] Floris Takens. Detecting strange attractors in turbulence. In *Dynamical Sys-*
901 *tems and Turbulence, Warwick 1980: proceedings of a symposium held at the*
902 *University of Warwick 1979/80*, pages 366–381. Springer, 2006.
- 903 [18] Jonathan Dushoff, Joshua B Plotkin, Simon A Levin, and David JD Earn.
904 Dynamical resonance can account for seasonality of influenza epidemics. *Pro-*
905 , 101(48):16915–16916, 2004.
- 906 [19] Alan Hastings, Carole L Hom, Stephen Ellner, Peter Turchin, and H Charles J
907 Godfray. Chaos in ecology: is mother nature a strange attractor? *Annual review*
908 *of ecology and systematics*, pages 1–33, 1993.
- 909 [20] Alan Hastings, Karen C Abbott, Kim Cuddington, Tessa Francis, Gabriel Gell-
910 ner, Ying-Cheng Lai, Andrew Morozov, Sergei Petrovskii, Katherine Scran-
911 ton, and Mary Lou Zeeman. Transient phenomena in ecology. *Science*,
912 361(6406):eaat6412, 2018.

- 913 [21] Matthew B Kennel, Reggie Brown, and Henry DI Abarbanel. Determining
914 embedding dimension for phase-space reconstruction using a geometrical con-
915 struction. *Physical review A*, 45(6):3403, 1992.
- 916 [22] Eugene Tan, Shannon Algar, Débora Corrêa, Michael Small, Thomas Stemler,
917 and David Walker. Selecting embedding delays: An overview of embedding
918 techniques and a new method using persistent homology. *Chaos: An Interdis-*
919 *ciplinary Journal of Nonlinear Science*, 33(3), 2023.
- 920 [23] Bjarke Frost Nielsen, Sang Woo Park, Emily Howerton, Olivia Frost Lorentzen,
921 Mogens H Jensen, and Bryan T Grenfell. Complex multiannual cycles of My-
922 coplasma pneumoniae: persistence and the role of stochasticity. *arXiv*, 2025.
- 923 [24] Samantha Bosis, Susanna Esposito, HGM Niesters, GV Zuccotti, G Marseglia,
924 Marcello Lanari, Giovanna Zuin, C Pelucchi, ADME Osterhaus, and Nicola
925 Principi. Role of respiratory pathogens in infants hospitalized for a first episode
926 of wheezing and their impact on recurrences. *Clinical microbiology and infection*,
927 14(7):677–684, 2008.
- 928 [25] Miguel L O’Ryan, Yalda Lucero, Valeria Prado, María Elena Santolaya, Marcela
929 Rabello, Yanahara Solis, Daniela Berriós, Miguel A O’Ryan-Soriano, Hector
930 Cortés, and Nora Mamani. Symptomatic and asymptomatic rotavirus and
931 norovirus infections during infancy in a Chilean birth cohort. *The Pediatric
932 infectious disease journal*, 28(10):879–884, 2009.
- 933 [26] Virginia E Pitzer, Cécile Viboud, Vladimir J Alonso, Tanya Wilcox, C Jessica
934 Metcalf, Claudia A Steiner, Amber K Haynes, and Bryan T Grenfell. Environmental
935 drivers of the spatiotemporal dynamics of respiratory syncytial virus in
936 the United States. *PLoS pathogens*, 11(1):e1004591, 2015.
- 937 [27] Arthur WD Edridge, Joanna Kaczorowska, Alexis CR Hoste, Margreet Bakker,
938 Michelle Klein, Katherine Loens, Maarten F Jebbink, Amy Matser, Cormac M
939 Kinsella, Paloma Rueda, et al. Seasonal coronavirus protective immunity is
940 short-lasting. *Nature medicine*, 26(11):1691–1693, 2020.
- 941 [28] Jennifer M Radin, Anthony W Hawksworth, Peter E Kammerer, Melinda Bal-
942 ansay, Rema Raman, Suzanne P Lindsay, and Gary T Brice. Epidemiology
943 of pathogen-specific respiratory infections among three US populations. *PLoS
944 One*, 9(12):e114871, 2014.
- 945 [29] Guojian Lv, Limei Shi, Yi Liu, Xuecheng Sun, and Kai Mu. Epidemiological
946 characteristics of common respiratory pathogens in children. *Scientific Reports*,
947 14(1):16299, 2024.
- 948 [30] Saverio Caini, Adam Meijer, Marta C Nunes, Laetitia Henaff, Malaika Zounon,
949 Bronke Boudewijns, Marco Del Riccio, and John Paget. Probable extinction of

- 950 influenza b/yamagata and its public health implications: a systematic literature
951 review and assessment of global surveillance databases. *The Lancet Microbe*,
952 2024.
- 953 [31] Zhiyuan Chen, Joseph L-H Tsui, Bernardo Gutierrez, Simon Busch Moreno,
954 Louis du Plessis, Xiaowei Deng, Jun Cai, Sumali Bajaj, Marc A Suchard,
955 Oliver G Pybus, et al. COVID-19 pandemic interventions reshaped the global
956 dispersal of seasonal influenza viruses. *Science*, 386(6722):eadq3003, 2024.
- 957 [32] Hai Nguyen-Tran, Sang Woo Park, Kevin Messacar, Samuel R Dominguez,
958 Matthew R Vogt, Sallie Permar, Perdita Permaul, Michelle Hernandez, Daniel C
959 Douek, Adrian B McDermott, et al. Enterovirus D68: a test case for the use of
960 immunological surveillance to develop tools to mitigate the pandemic potential
961 of emerging pathogens. *The Lancet Microbe*, 3(2):e83–e85, 2022.
- 962 [33] Bryan T Grenfell, Ottar N Bjørnstad, and Bärbel F Finkenstädt. Dynamics of
963 measles epidemics: scaling noise, determinism, and predictability with the TSIR
964 model. *Ecological monographs*, 72(2):185–202, 2002.
- 965 [34] Samit Bhattacharyya, Per H Gesteland, Kent Korgenski, Ottar N Bjørnstad,
966 and Frederick R Adler. Cross-immunity between strains explains the dynamical
967 pattern of paramyxoviruses. *Proceedings of the National Academy of Sciences*,
968 112(43):13396–13400, 2015.
- 969 [35] Katharine R Dean, Fabienne Krauer, Lars Walløe, Ole Christian Lingjærde, Bar-
970 Barbara Bramanti, Nils Chr Stenseth, and Boris V Schmid. Human ectoparasites
971 and the spread of plague in Europe during the Second Pandemic. *Proceedings
972 of the National Academy of Sciences*, 115(6):1304–1309, 2018.
- 973 [36] Margarita Pons-Salort and Nicholas C Grassly. Serotype-specific immunity
974 explains the incidence of diseases caused by human enteroviruses. *Science*,
975 361(6404):800–803, 2018.
- 976 [37] Sarah Cobey and Edward B Baskerville. Limits to causal inference with state-
977 space reconstruction for infectious disease. *PloS one*, 11(12):e0169050, 2016.
- 978 [38] P Rohani, CJ Green, NB Mantilla-Beniers, and Bryan T Grenfell. Ecological
979 interference between fatal diseases. *Nature*, 422(6934):885–888, 2003.
- 980 [39] Sema Nickbakhsh, Colette Mair, Louise Matthews, Richard Reeve, Paul CD
981 Johnson, Fiona Thorburn, Beatrix Von Wissmann, Arlene Reynolds, James
982 McMenamin, Rory N Gunson, et al. Virus–virus interactions impact the popu-
983 lation dynamics of influenza and the common cold. *Proceedings of the National
984 Academy of Sciences*, 116(52):27142–27150, 2019.

- 985 [40] Neil Ferguson, Roy Anderson, and Sunetra Gupta. The effect of antibody-
986 dependent enhancement on the transmission dynamics and persistence of
987 multiple-strain pathogens. *Proceedings of the National Academy of Sciences*,
988 96(2):790–794, 1999.
- 989 [41] Public Health Agency of Canada. Respiratory virus detections in
990 Canada. 2024. <https://www.canada.ca/en/public-health/services/surveillance/respiratory-virus-detections-canada.html>. Accessed Sep
991 4, 2024.
- 993 [42] Centre for Health Protection. Detection of pathogens from respiratory spec-
994 imens. 2024. <https://www.chp.gov.hk/en/statistics/data/10/641/642/2274.html>. Accessed Nov 20, 2024.
- 996 [43] Centre for Health Protection. Detection of gastroenteritis viruses from faecal
997 specimens. 2024. <https://www.chp.gov.hk/en/statistics/data/10/641/717/3957.html>. Accessed Nov 20, 2024.
- 999 [44] Korea Disease Control and Prevention Agency. Acute respiratory infection,
1000 Sentinel surveillance infectious diseases. 2024. <https://dportal.kdca.go.kr/pot/is/st/ari.do>. Accessed Nov 20, 2024.
- 1002 [45] Edward Goldstein, Sarah Cobey, Saki Takahashi, Joel C Miller, and Marc Lipsitch.
1003 Predicting the epidemic sizes of influenza A/H1N1, A/H3N2, and B: a
1004 statistical method. *PLoS medicine*, 8(7):e1001051, 2011.
- 1005 [46] Karline Soetaert, Thomas Petzoldt, and R Woodrow Setzer. Solving differential
1006 equations in R: package deSolve. *Journal of statistical software*, 33:1–25, 2010.
- 1007 [47] R Core Team. *R: A Language and Environment for Statistical Computing*. R
1008 Foundation for Statistical Computing, Vienna, Austria, 2023.
- 1009 [48] Sang Woo Park, Inga Holmdahl, Emily Howerton, Wenchang Yang, Rachel E
1010 Baker, Gabriel A Vecchi, Sarah Cobey, C Jessica E Metcalf, and Bryan T Grenfell.
1011 Interplay between climate, childhood mixing, and population-level suscep-
1012 tibility explains a sudden shift in RSV seasonality in Japan. *medRxiv*, pages
1013 2025–03, 2025.
- 1014 [49] Bob Carpenter, Andrew Gelman, Matthew D Hoffman, Daniel Lee, Ben
1015 Goodrich, Michael Betancourt, Marcus A Brubaker, Jiqiang Guo, Peter Li,
1016 and Allen Riddell. Stan: A probabilistic programming language. *Journal of
1017 statistical software*, 76, 2017.
- 1018 [50] Stan Development Team. RStan: the R interface to Stan, 2024. R package
1019 version 2.32.6.